

# Parsec-scale obscuring accretion disk with large scale magnetic field in AGN

A. Dorodnitsyn<sup>1,2,3</sup>, T. Kallman<sup>1</sup>

## ABSTRACT

Magnetic field dragged from the galactic disk along with inflowing gas can provide vertical support to the geometrically and optically thick pc-scale torus in AGN. Using the Soloviev solution initially developed for Tokamaks we derive an analytical model for a rotating torus supported and confined by magnetic field. We further perform three-dimensional magneto-hydrodynamics simulations of X-ray irradiated pc-scale magnetized tori. We follow the time evolution and compare models which adopt initial conditions derived from our analytic model with simulations in which the initial magnetic flux is entirely contained within the gas torus. Numerical simulations demonstrate that the initial conditions based on the analytic solution produce a longer-lived torus and one which produces obscuration which is generally consistent with observed constraints.

## 1. Introduction

The unification paradigm of Active Galactic Nuclei (AGN) implies the existence of a geometrically thick belt of matter which wraps and hides the inner, most luminous region of AGN from viewing close to the equatorial plane (Antonucci 1984; Antonucci & Miller 1985; Rowan-Robinson 1977). This can explain the dichotomy of Type I and Type II AGNs and Quasars, attributing their differing appearance to the geometrical positioning of an AGN with respect to an observer.

Observations favor this model, but the mechanism that actually supports such a geometrically thick structure is not determined. In the absence of efficient cooling, the virial theorem predicts that gas which is orbiting the black hole at the radius of the putative

---

<sup>1</sup>Laboratory for High Energy Astrophysics, NASA Goddard Space Flight Center, Code 662, Greenbelt, MD, 20771, USA

<sup>2</sup>University of Maryland, Baltimore County (UMBC/CRESST), Baltimore, MD 21250, USA

<sup>3</sup>Space Research Institute, 84/32, Profsoyuznaya st., Moscow, Russia

torus,  $r \simeq 1$  pc will have temperature  $T_{\text{vir,g}} \simeq 10^6$  K for a  $10^7 M_{\odot}$  black hole. Dust at such temperatures is destroyed by sputtering, while the presence of dust in the torus is supported by abundant observational evidence. Emission from warm dust manifests itself in a broad hump in the spectral energy distribution (SED) in the  $\sim 1 - 10\mu$  wavelength band (Rieke & Lebofsky 1981; Barvainis 1987; Sanders et al. 1989; Pier & Krolik 1993). Interferometric observations provide direct evidence of warm, multi-temperature dust at parsec scales in a growing sample of nearby type II and type I AGNs, including NGC 1068 (Poncellet et al. 2006; Raban et al. 2009; Wittkowski et al. 2004; Jaffe et al. 2004) the Circinus galaxy (Tristram et al. 2007, 2014) and others (Kishimoto et al. 2013; Hönig et al. 2012; Meisenheimer et al. 2007; Beckert et al. 2008). Observations of ionization and scattering cones also indicate the existence of a toroidal obscuring structure (eg. Pogge & De Robertis 1993; Wilson 1996; Zakamska et al. 2005).

Obscuration could be provided by a globally warped but intrinsically geometrically thin disk (Phinney 1989; Sanders et al. 1989). A disk that is severely warped at parsec scales may also be the result of stochastic accretion, i.e. accretion that proceeds from random directions (Lawrence & Elvis 2010; Hopkins et al. 2012). Numerical simulations which support this scenario, and follow AGN fueling from galactic scales (eg. Hopkins et al. 2005; Hopkins & Quataert 2010; Hopkins et al. 2012), are very demanding and thus are somewhat restricted in the ways they take into account effects of magnetic fields or radiation transfer. When they provide geometrically thick inflows the gas temperature always resides at a significant fraction of  $T_{\text{vir,g}}$ . UV and IR radiation pressure on dust may provide the necessary vertical support. The temperature of such a torus will be of the order of the "radiation virial temperature"  $T_{\text{vir,r}} \simeq 10^3 (n_7 M_7 / r_{\text{pc}})^{1/4}$  K  $\ll T_{\text{vir,g}}$ , where  $n = 10^7 n_7 \text{ cm}^{-3}$  is the number density and  $M_{\text{BH}} = 10^7 M_7 M_{\odot}$  is the mass of the Black Hole, and  $r_{\text{pc}}$  is the radius in parsecs.

Several such models have been proposed: a static torus: (Krolik 2007; Shi & Krolik 2008) as well as models in which the torus is dynamic - "windy torus": (Dorodnitsyn et al. 2011), (Dorodnitsyn et al. 2012; Dorodnitsyn & Kallman 2012; Chan & Krolik 2016). Simulations show that IR pressure support works most efficiently in AGNs with inferred bolometric luminosity  $L \gtrsim 0.1 L_{\text{edd}}$ , where  $L_{\text{edd}}$  is the Eddington luminosity.

The torus is also the most likely source of gas for the inner accretion disk and the fueling of the black hole. This raises the important question of the nature of the mechanism that provides angular momentum redistribution. This includes the mechanism which operates on scales larger than the torus, and brings gas into the torus, and also the mechanisms operating within the torus.

On galactic scales, gas can be funneled towards the center as a result of a galaxy merger, leading to the development of the bar instability ( Shlosman et al. 1989, 1990). Observations

indicate the existence of large scale magnetic fields on galactic scales (i.e. Beck & Wielebinski 2013; Beck 2011), and the inflow can transport magnetic flux from the inner parts of the host galaxy towards the torus. The importance of magnetic flux can be inferred from the following approximate arguments: assume the spherically-symmetric shell of gas located within the BH sphere-of-influence, falls radially at roughly a free-fall velocity and with a constant accretion rate. Then assuming perfect conductivity, conservation of magnetic flux implies  $B_r \sim r^{-2}$ , where  $B_r$  is the radial component of the magnetic field. The gas internal energy scales as  $\rho v^2/2 \sim r^{-5/2}$ . The density profile is then  $\rho \sim r^{-3/2}$  and the distance from the BH where magnetic field becomes dynamically important can be estimated from energy equipartition arguments (Bisnovatyi-Kogan & Ruzmaikin 1974; Bisnovatyi-Kogan & Lovelace 2000):  $r_m = r_{\text{out}}^{8/3} B_{\text{out}}^{4/3} \dot{M}_{\odot}^{-2/3} (GM_{\text{BH}})^{-1/3} \simeq 81 B_{10}^{4/3} R_{100}^{8/3} \dot{m}_{0.01}^{-2/3} M_7^{-1/3} \text{pc}$ , where  $B_{10}$  is the galactic magnetic field scaled to  $10 \mu\text{G}$ ,  $R_{100}$  is the outer AGN radius  $r_{\text{out}}$  in units of 100 pc, the accretion rate,  $\dot{m}_{0.01}$  is scaled to  $10^{-2} M_{\odot}/\text{yr}$ , and  $M_7$  is the mass of the BH in  $10^7 M_{\odot}$ . Parsec-scale magnetic field loops that were small-scale in the galactic disk will dominate the geometry in the torus region. This illustrates the potential dynamical importance of magnetic field in the torus. If so, in such a magnetized rotating torus, orbital shear can lead to magnetic instability in which angular momentum is redistributed via magnetic stresses.

In AGN disks various angular momentum transport mechanisms are likely to operate at different scales. Long-range non-axisymmetric gravitational torques acting in the stellar and gas system can be responsible for angular momentum transport on galactic scales (Lynden-Bell & Kalnajs 1972). Theoretical results (Shlosman et al. 1989, 1990) along with the results of numerical simulations (Hopkins et al. 2012) suggest that global non-axisymmetric instabilities are capable of siphoning significant amounts of gas towards a central AGN. A different regime is established if the gas cooling time is comparable to the dynamical time  $\simeq \Omega^{-1}$ . Such gas settles into a "gravito-turbulent state" which is characterized by the non-linear development of self-gravitating instabilities which provide dissipation and stresses, eventually leading to angular momentum transport (i.e. Paczynski 1978; Gammie 2001; Goodman 2003; Rafikov 2009).

In the inner accretion disk MHD turbulence driven by the MRI instability (Balbus & Hawley 1991) is currently the most likely mechanism for angular momentum transport leading to accretion. Significant insight here comes from local, shearing box simulations. An important result of such simulations is that the presence of net magnetic flux in the simulation box essentially guarantees the efficacy of the MRI. It has been shown (Fromang & Papaloizou 2007), that in the absence of such net magnetic flux, the saturated level of magnetic stresses due to MRI decreases with increasing numerical resolution. Further simulations in shearing boxes showed that preexisting net large-scale magnetic flux not only increases MRI-driven turbulence but could be a necessary ingredient for the saturation of MRI-stresses at a level

relevant to angular transport in standard  $\alpha$  disks (Shi et al. 2016; Hawley et al. 1995; Sano et al. 2004; Simon et al. 2009; Guan et al. 2009). These results imply that the magnetic flux advected from the galaxy can enhance turbulent transport in the torus.

Shearing box simulations cannot assess non-local coupling between distant disk regions. Such non-locality can be provided by large-scale field connecting different patches of the disk, and can only be addressed via global simulations. The potential effect of large scale fields on accretion dynamics have been pointed out by early theoretical (Bisnovatyi-Kogan & Ruzmaikin 1974) and numerical (Igumenshchev et al. 2003; Narayan et al. 2003) studies. Current understanding of angular momentum transport and MHD turbulence connects the results from global and local simulations (e.g. Hawley et al. 2013; Sorathia et al. 2012). One insight is the importance of accumulation of the vertical magnetic flux in the inner parts of the disk - an effect with a potential to significantly affect accretion leading to a “magnetically arrested disk” (e.g. Igumenshchev 2008; Beckwith et al. 2009; Suzuki & Inutsuka 2014; Avara et al. 2016; Beckwith et al. 2011; McKinney et al. 2012)

Surprisingly little effort has been devoted to the investigation of the role of large scale magnetic fields in the context of the AGN outer disk/torus. Lovelace et al. (1998) derived a model of a magnetically-supported, thick torus assuming that the magnetic field is produced by an equatorial current loop and making a number of other simplifications suitable for an approximate analytic model. A different class of magnetic models associate the torus with a geometrically thick flow, driven either by magnetic driving (Konigl & Kartje 1994; Elitzur & Shlosman 2006; Fukumura et al. 2010) alone, or in combination with radiation pressure (Emmering et al. 1992; Everett 2005; Keating et al. 2012). To launch the wind these models rely on an ordered global magnetic field with foot-points originating on a thin disk.

To explore conditions needed to produce obscuration and outflows, and to address the effect of anomalous angular momentum transport Dorodnitsyn et al. (2016) performed viscous radiation hydrodynamics simulations. These simulations show that the obscuring torus can effectively supply the inner accretion disc with gas, being at the same time geometrically thick due to radiation pressure of IR on dust and X-ray heating. An effective viscosity was adopted to disguise unknown details of self-gravity and magnetic stresses. This approach however cannot mimic the role of large scale magnetic field. A complementary study (Chan & Krolik 2016) treated a weakly magnetized torus exposed to external UV radiation. They did not take into account X-ray heating and dust evaporation in the low density regions of the torus such as in the torus funnel. Despite these differences the results of these simulations are broadly consistent with the results of Dorodnitsyn et al. (2011, 2012) who concluded that at high AGN luminosity the torus dynamics is largely determined by just two parameters: radiation input and high dust opacity.

The effect of global field geometry on disk structure has been studied in the context of formation of jets and winds (Beckwith et al. 2009). Various assumptions about the initial field geometry and its effects on the net accretion rate have been explored by McKinney and Blandford (2009) and Beckwith et al. (2008). In the context of the pc-scale torus, an important question is the relation of the global field to the torus aspect ratio and its ability to provide obscuration. The study of this question is primary goal of this paper.

The properties of the torus depend on the interplay between radiation, hydrodynamics, gravity and magnetic field. Our program so far has been to include the first two of these. It is the goal of the current paper to test the effects of global magnetic field on the structure and evolution of the torus, by treating the torus essentially as a magnetized accretion disk exposed to external irradiation. In this paper we will be exploring models for the torus which include magnetic fields and X-rays heating but do not include any other radiation effects.

Observational evidence suggests that the distribution of hot dust in AGN scales with the square root of the luminosity (Barvainis 1987; Tristram & Schartmann 2011; Suganuma et al. 2006; Kishimoto et al. 2011; Weigelt et al. 2012; López-Gonzaga & Jaffe 2016, i.e.) The connection of the inner torus to the BLR (i.e. Netzer & Laor 1993) was probed in (e.g. Czerny & Hryniewicz 2011; Czerny et al. 2004). In our previous research that involved radiation-hydrodynamics studies of AGN torus, dust sublimation radius appeared as a natural scale of the AGN along with the fact that complicated radiation transfer effects intervene in a significant way. In the current work we are interested mainly in the effects of the magnetic fields and no dust or radiation pressure on dust is considered. Correspondingly, our current studies do not contain any such scale as the dust sublimation radius.

The plan of the paper is as follows: In the first part we study an analytic model of a magnetically supported torus. Our approximate solution is based on the exact solution of the Grad-Shafranov equation - the solution initially derived by Soloviev for the toroidal equilibrium in Tokamaks. This part of the paper is complimentary to the second where we perform three- dimensional numerical simulations of the X-ray illuminated torus threaded by global magnetic field. We compare simulations using initial conditions based on our analytic model with simulations using initial conditions in which the initial field is entirely within the torus gas. We show that the evolution of a physically realistic torus is sensitive to these assumptions about the global field distribution, and that this affects the obscuring properties as well. In the results section we summarize many of the characteristics of the torus such as its dynamics, obscuring properties, accretion-rate etc. We conclude with discussion of the implications of our models for understanding the torus dynamics, and potential limitations associated with the our assumptions.

## 2. MHD Equations for AGN Torus

We model the torus using three-dimensional, ideal MHD equations describing magnetized gas susceptible to radiative heating and cooling in a Newtonian gravitational potential:

$$\partial_t \rho + \nabla \cdot (\rho \mathbf{v}) = 0, \quad (1)$$

$$\partial_t(\rho \mathbf{v}) + \nabla \cdot (\rho \mathbf{v} \mathbf{v} - \mathbf{B} \mathbf{B} + P^* \mathbf{I}) = -\rho \frac{G M_{\text{BH}}}{r^2} \hat{\mathbf{r}}, \quad (2)$$

$$\partial_t E + \nabla \cdot [(E + P^*) \mathbf{v} - \mathbf{B}(\mathbf{B} \cdot \mathbf{v})] = -\rho \mathbf{v} \cdot \frac{G M_{\text{BH}}}{r^2} \hat{\mathbf{r}} - \rho \mathcal{L}, \quad (3)$$

$$\partial_t \mathbf{B} + \nabla \cdot (\mathbf{v} \cdot \mathbf{B} - \mathbf{B} \cdot \mathbf{v}) = 0, \quad (4)$$

where density,  $\rho = n m_{\text{u}} \mu$  ( $m_{\text{u}} = 1 \text{ amu} \simeq m_p$  is the atomic mass unit;  $m_p$  is the proton's mass); we also adopt  $\mu = 1$  for the mean mean molecular weight.  $P^* \equiv P + (\mathbf{B} \cdot \mathbf{B})/2$  is the total pressure,  $E$  is the total energy density,  $E \equiv e + \rho(\mathbf{v} \cdot \mathbf{v})/2 + (\mathbf{B} \cdot \mathbf{B})/2$ , where  $e$  is the internal energy density. A polytropic equation of state is assumed:  $P = (\gamma - 1) e$ , where  $P$  is the gas pressure,  $\gamma$  is the ratio of specific heats. Additional notation includes  $r$ , and  $\hat{\mathbf{r}}$  - the usual spherical radius and the spherical radial unit vector. Interaction with radiation is included in the form of the X-ray cooling-heating function,  $\mathcal{L}$  [ $\text{erg g}^{-1} \text{s}^{-1}$ ] in (3) (see Section 2.2). In Section 3 we provide numerical solution to these equations (1)–(4). As a prelude, we first discuss equilibrium solutions for a magnetic torus.

### 2.1. Soloviev solution for the magnetically-confined torus

For an illustration of the possibility of magnetic torus support, we notice that analytic estimates for the torus density distribution can be made upon making several simplifying assumptions: i) the torus is stationary, and ii) axially-symmetric. The latter implies that the dependence on the three components of the magnetic field can be reduced to the dependence on a single scalar function (see the Appendix) for which one can take a magnetic flux through the circle of a radius,  $R$ :

$$\Psi(R, z) = \frac{1}{2\pi} \int \mathbf{B} \cdot \mathbf{n} ds = A_\phi R, \quad (5)$$

where  $\mathbf{n}$  is the normal vector to the equatorial plane,  $A_\phi$  is the  $\phi$ -component of the vector potential. Then the magnetic field can be expressed as

$$\mathbf{B} = \frac{I}{R} \hat{\phi} + \frac{\nabla\Psi \times \hat{\phi}}{R}, \quad (6)$$

where  $I = RB_\phi$  is the poloidal current, and  $\hat{\phi}$  is the unit vector in  $\phi$  direction.

In a seminal work, Soloviev (Leontovich 1975) gives an approximate solution to the problem of toroidal equilibrium in Tokamaks. Considering a non-rotating, magnetically confined and gas supported torus, Soloviev solves the corresponding Grad-Shafranov force balance equation (see the Appendix). He argues that the flux function,  $\Psi(R, z)$  in such a case can be expanded around the magnetic axis in a power series of  $(R^2 - R_0^2)/R_0^2$  and  $z^2/R_0^2$ , where  $R_0$  is the cylindrical radius of the magnetic axis. On the magnetic axis, i.e. at  $R = R_0$ ,  $z = 0$  it should satisfy  $\partial_R\Psi = \partial_z\Psi = 0$ . An additional condition is provided by the requirement that  $\Psi$  should be symmetrical with respect to the equatorial plane. The resultant solution to the Grad-Shafranov equations can be cast in the form:

$$\Psi(R, z) = z^2 (a_1 (R^2 - R_0^2) + b_1) + a_2 (R^2 - R_0^2)^2, \quad (7)$$

where  $a_1$ ,  $a_2$ , and  $b_1$  are parameters. Figure 1 shows contour plots of  $\log \Psi$ , poloidal field,  $\mathbf{B}_p$ , and  $\log P_m$  where  $P_m = B^2/8\pi$  is the magnetic pressure. A class of solutions was found by Soloviev, assuming that,  $\frac{dP}{d\Psi} = Const$ . If so, parameters  $a_1$ ,  $a_2$ , and  $b_1$  are found upon substitution to the Grad-Shafranov equation (Leontovich 1975). Rotation was included into the Soloviev-type solution by Maschke & Perrin (1980); To include rotation in this scheme it was found that it is necessary to adopt a significant number of further additional simplifications. The geometry of the  $\Psi = const$ . surfaces can be complex: Depending on the parameters, a second magnetic axis can be found at the origin of the coordinate system; hyperbolic points can occur at the intersection of the separatrices, etc. These are important for the stability of the Tokamak, although in the case of an accretion disk such fine details of the initial distribution of the magnetic field are quickly “forgotten” by the turbulent solution.

In this work we take a different approach. From the theory of magnetically-driven winds it is known that moving gas in the magnetic field should conform to certain integrals of motion. For example, the equation of motion can be projected onto the direction of the poloidal magnetic field,  $\mathbf{B}_p$  to obtain the first integral (e.g. Spruit (1996)):

$$\text{Br}(\Psi) = \frac{v_p^2}{2} + \frac{(v_\phi - \Omega(\Psi)R)^2}{2} + H + \Phi - \frac{\Omega(\Psi)^2 R^2}{2}, \quad (8)$$

where  $H$  is the enthalpy (defined by the equation (A11) in Appendix),  $\Phi$  is the gravitational potential,  $v_p$  is the poloidal, and  $v_\phi$  is the azimuthal components of the velocity. The

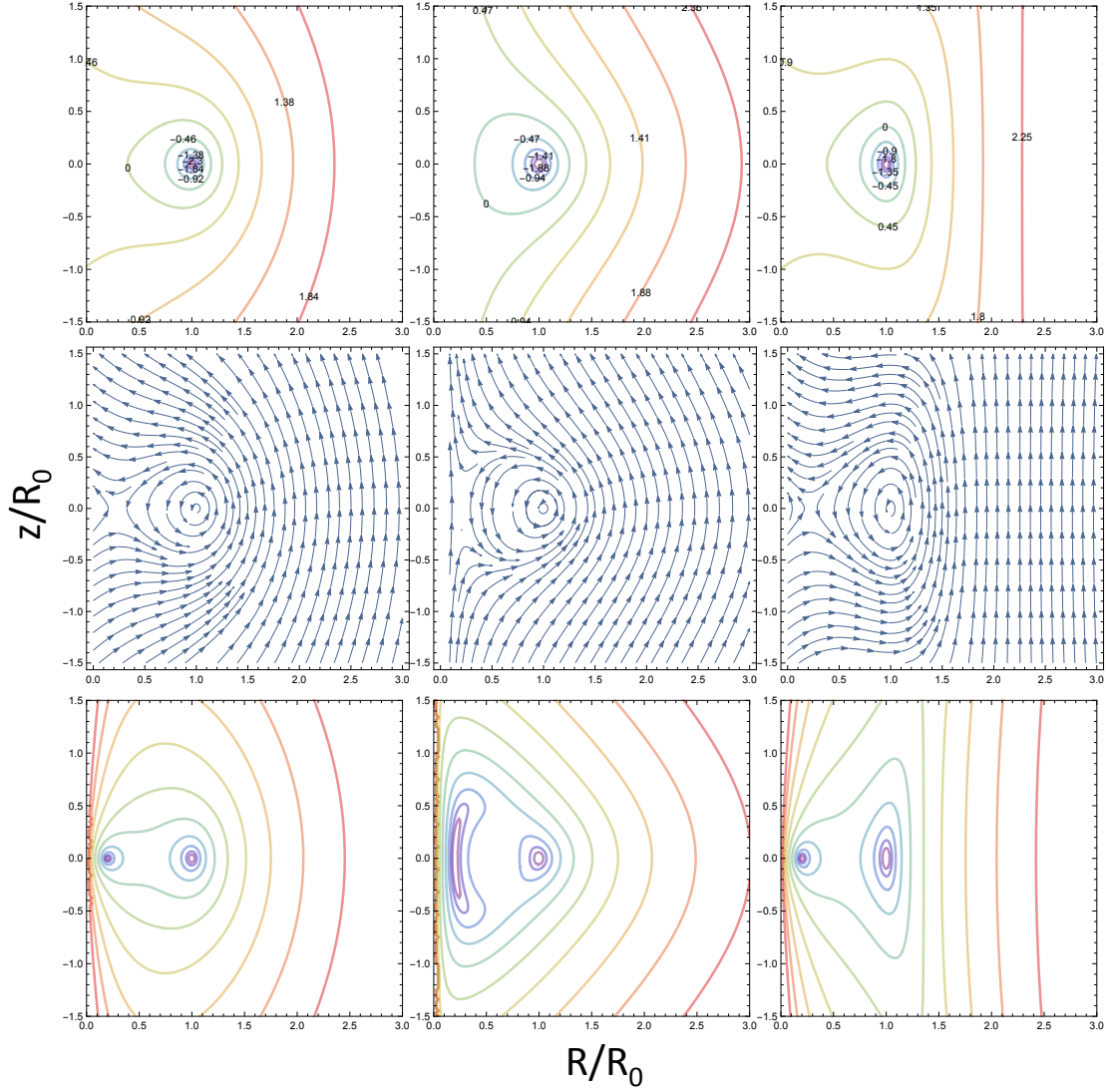


Fig. 1.— Flux function,  $\log \Psi$  (upper), magnetic field, (middle), and magnetic pressure,  $\log P_m$  (lower) panel. Axes: horizontal:  $R/R_0$ ; vertical:  $z/R_0$ , where  $R_0$  is the radius of the magnetic axis. Parameters  $a_1, a_2, b_1$  from (7) are fixed for all plots in a column: left column:  $a_1 = 1, a_2 = 1, b_1 = 3$ ; middle column:  $a_1 = 3, a_2 = 1, b_1 = 3$ ; right column:  $a_1 = -1, a_2 = 3, b_1 = 4$ .



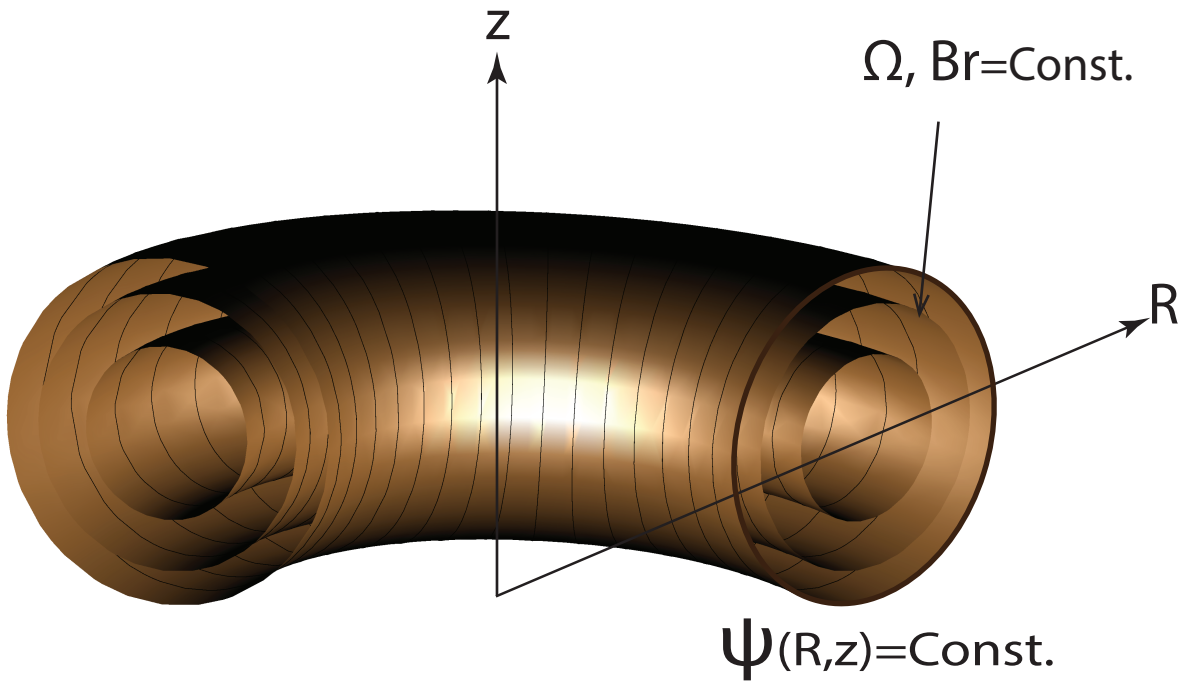


Fig. 2.— A sketch of a segment of the torus composed of the of nested magnetic flux surfaces,  $\Psi$  from (5). Gas that belongs to a particular flux surface has a fixed value of angular velocity,  $\Omega(\Psi)$  and Bernoulli function,  $Br(\Psi)$  from (8). Thin lines mark the poloidal magnetic field,  $\mathbf{B}_p$ .

Bernoulli-like function,  $\text{Br}[\text{erg} \cdot \text{g}^{-1}]$  is constant on a given flux surface  $\Psi$ . In the situation considered here the gas “lives” on a given closed magnetic field line, in the  $\{R, z\}$  plane (see Figure 2). Notice that  $\Omega(\Psi)$  is the rotation rate of the magnetic field foot point. In a stationary toroid a closed magnetic field line must co-rotate with the gas, i.e.  $v_\phi = \Omega R$  and hence with the foot point of the corresponding magnetic field line. In general, the gas can have a nonzero poloidal velocity,  $v_p$  in which case such large-scale poloidal motions resemble meridional circulation in stationary rotating stars (Tassoul 1978). Here we assume that there is no meridional circulation. Equation (8) is reduced to

$$\text{Br}(\Psi) = H + \Phi - \frac{\Omega^2 R^2}{2}, \quad (9)$$

where as before  $\text{Br}(\Psi)$  is constant on a given flux surface. In the original Soloviev solution  $P'(\Psi) = \text{Const.}$  Making use of this insight we can assume that, since  $\Omega(\Psi)$  and  $\text{Br}(\Psi)$  are both constants on a given surface of  $\Psi = \text{Const.}$ , we can make the following approximation:

For convenience we scale all the variables to their corresponding values at the equatorial plane at  $R = R_0$ :  $\tilde{x} = R/R_0$ ,  $\tilde{z} = z/R_0$ , and  $\tilde{\rho} = \rho/\rho_0$ ;  $\tilde{P} = P/P_0$ , where  $P_0 = \rho_0 U_0^2$ ,  $U_0^2 = GM/R_0$ ,  $\tilde{\Omega} = \Omega/\Omega_0$ , where  $\Omega_0 = U_0/R_0$ ;  $\tilde{\text{Br}} = \text{Br}/U_0^2$ ,  $\tilde{\Psi} = \Psi/\Psi_0$  where  $\Psi_0$  is an arbitrary scale factor. We henceforth adopt these non-dimensional variables and for convenience dropping the tilde:

$$\Omega^2 = 1 - \omega_1^2 \Psi, \quad (10)$$

$$\text{Br} = 1 - \text{Br}_1 \Psi, \quad (11)$$

where  $\omega_1$ ,  $\text{Br}_1$  are parameters. Adopting polytropic gas, and transforming  $H$  accordingly (see Appendix) we obtain from (8):

$$\rho = \frac{1}{\tilde{K}(1+n)} \left( 1 + \frac{1}{(x^2 + z^2)^{1/2}} + \frac{x^2}{2}(1 - w_1 \Psi(x, z)) - \text{Br}_1 \Psi(x, z) \right). \quad (12)$$

where  $\tilde{K} = (\text{Br}_0 + 3/2)/(n+1)$ , and  $n = 1/(\gamma - 1)$  is the index of the polytrope. A contour plot of the density in the  $x, z$  plane obtained from (12) is shown in Figure 3. It features both a magnetized torus and a quasi-spherical region near the center. We do not consider the latter part of the solution in the current work.

Analytical solution of the Grad-Shafranov equation exists only in a small number of situations which are relevant to astrophysics. When they exist they can sometimes provide useful insight into the properties of axially-symmetric, equilibrium configurations. Numerical solution of the equation can be equally complex, as the positions of the critical points/surfaces are not known and should be found during the solution (see the discussion in Beskin (2009))

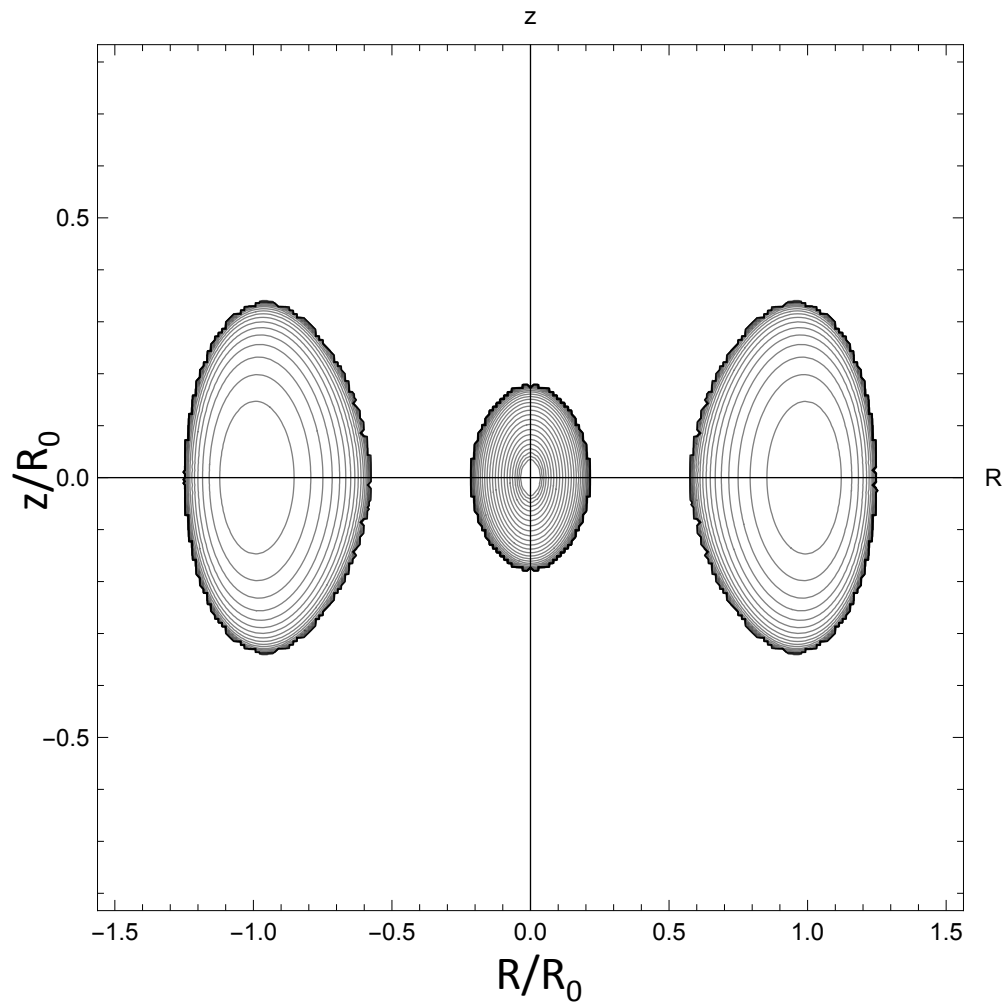


Fig. 3.— Density contours,  $\log \rho$  from equation (12) for parameters  $Br_1 = 6$ ,  $w_1 = 2$ .

and references therein). In the subsequent sections we adopt the solution (12) as an initial input to a full time-dependent numerical solution to the MHD equations in an AGN torus.

## 2.2. Effects of X-ray Illumination

In luminous AGN, tori are subject to strong X-ray illumination. Our numerical torus models include the effects of illumination, and in what follows we discuss its role in affecting the torus structure and evolution. To model the effects of X-ray illumination, we treat the external continuum as being produced by the corona at the inner parts of the accretion disk. To isolate the effect that the X-rays play on the dynamics of the flow, we do not consider the influence of UV flux (see Discussion). Optical depth along the spherical radius  $r$  is adopted to calculate the attenuation of the incident X-ray flux:  $\tau_x = \int \kappa_x \rho dr$ , where  $\kappa_x$  is the X-ray opacity which we take to be equal to the Thomson opacity.

Then  $F_X = F_{X,0} \exp(-\tau_X)$ , where  $F_{X,0} = L_X/4\pi r^2$  is the local X-ray flux, and  $L_X$  is the luminosity of the nucleus in X-rays. We assume that a fraction  $L_X = f_x L_a$  is radiated in X-rays from the total accretion luminosity,  $L_a = \Gamma L_{\text{edd}}$ , where the latter also serves as a definition of  $\Gamma$  –the important free parameter of the problem;  $L_{\text{edd}} = 1.25 \cdot 10^{45} M_7$  is the Eddington critical luminosity where  $M_7$  is the mass of a BH in  $10^7 M_\odot$ .

We assume that the ionization state of the gas and the heating and cooling rates are in time-steady equilibrium and therefore the quantities in (3) are functions of the ionization parameter:

$$\xi = 4\pi F_x/n \simeq 4 \cdot 10^3 \cdot f_x \Gamma M_7 / (N_{23} r_{\text{pc}}), \quad (13)$$

where  $N_{23}$  is the column density in  $10^{23} \text{ cm}^{-2}$ . The approach taken in this work with respect to X-ray heating and cooling is similar to our previous studies (e.g. Dorodnitsyn et al. 2016).

The heating and cooling function that appears in (3) can be written:

$$\mathcal{L} = \frac{n}{\mu m_p} (\Lambda - H_X). \quad (14)$$

Heating and cooling rates are calculated making use of the XSTAR photo-ionization code (Kallman & Bautista 2001) assuming ionizing continuum with (energy) power law index of  $\alpha=1$ . We further use analytical approximations of the above rates similar to those used by Blondin (1994)

$$H_X = H_{\text{PI}} + H_{\text{IC}}, \quad (15)$$

where  $H_{\text{PI}}$  is the photo-ionization heating-recombination cooling:

$$H_{\text{PI}}(\text{erg cm}^3 \text{ s}^{-1}) = 1.5 \cdot 10^{-21} \xi^{1/4} T^{-1/2} (T_x - T) T_x^{-1}, \quad (16)$$

as well as Compton heating and cooling,  $H_{\text{IC}}$ :

$$H_{\text{IC}}(\text{erg cm}^3 \text{ s}^{-1}) = 8.9 \cdot 10^{-36} \xi (T_x - 4T), \quad (17)$$

The cooling rate also includes bremsstrahlung and line cooling:

$$\begin{aligned} \Lambda(\text{erg cm}^3 \text{ s}^{-1}) &= 3.3 \cdot 10^{-27} T^{1/2} \\ &+ (4.6 \cdot 10^{-17} \exp(-1.3 \cdot 10^5/T) \xi^{(-0.8-0.98\alpha)} T^{-1/2} + 10^{-24}) \delta. \end{aligned} \quad (18)$$

The parameter  $\delta$  regulates the relative importance of optically line cooling (Blondin 1994). We take the parameter  $\delta \simeq 1$  representing optically thin line cooling. Formulas (17)-(18) are the versions used by Dorodnitsyn et al. (2008). When compared with the values in Blondin (1994) the updated results reflect newer atomic data and the choice of a power law ionizing spectral energy distribution.

### 3. Numerical Solution

#### 3.1. Methods

We further investigate the evolution of a magnetized torus exposed to external X-ray illumination via three-dimensional numerical simulations. To solve a system of equations of ideal magnetohydrodynamics (1)–(4), we adopt the second-order Godunov code *Athena* (Stone et al. 2008). The code is configured to adopt a uniform cylindrical grid,  $\{R_i, \phi_j, z_k\}$ , (Skinner & Ostriker 2010).

Simulations are performed in a static Newtonian gravitational potential. The van Leer integrator is found to be the most robust choice for the simulations presented in this work. We implement the heating and cooling term in the same way as the static gravitational potential source term is implemented in the current van Leer integrator implementation in *Athena*. That is, the heating source term is implemented to guarantee 2-nd order accuracy in both space and time.

Given the large parameter space and numerical cost of simulations involving X-ray heating we postpone an extensive investigation of the parameter space to future work. Correspondingly, we present a comparative analysis of two models: a torus that initially contains

all of the magnetic flux inside its body; and a torus which along with field in its body is embedded in a large scale magnetic field of the type described by the approximate analytic solutions to the Grad-Shafranov equation from Section 2.1.

### 3.2. Initial conditions: TOR and SOL

The two initial setups for numerical simulations differ according to the assumptions about the initial magnetic field permeating the computational domain. In the first case, the magnetic field is completely embedded into the initial toroidal gas configuration (hereafter TOR); In the second setup (hereafter SOL), the initial magnetic field is calculated from the Soloviev parametrization of the flux function,  $\Psi$ , inside the torus. The initial magnetization, in both cases is assumed to be small. Notice that this assumption does not preclude the formation of highly magnetized regions in the course of the simulation.

The TOR setup is similar to previous accretion disk simulations, such as Hawley (2000); Hawley & Krolik (2001). Such a torus is entirely gas pressure-supported, with angular velocity,  $\Omega$  that is constant on cylinders:

$$\Omega \sim R^{-q}, \tag{19}$$

where, for example,  $q = 3/2$  corresponds to Keplerian motion in the equatorial plane; a torus with constant angular momentum corresponds to  $q = 2$ . In cylindrical coordinates, in an axially symmetrical case, an equilibrium distribution of polytropic gas inside rotating torus can be found analytically (Papaloizou & Pringle 1984):

$$\frac{\gamma}{\gamma - 1} \frac{P}{\rho} - \frac{1}{(x^2 + z^2)^{1/2}} - \frac{x^{-2q+2}}{2 - 2q} = Const, \tag{20}$$

where non-dimensional variables from Section 2.1 are adopted.

In both the initial TOR and SOL setups only the poloidal components of the magnetic field (i.e.  $B_x$  and  $B_z$ ) are taken into account. The initial toroidal field in both setups is set to zero. To calculate  $B_x$ , and  $B_z$  in the TOR setup, it is assumed that inside the torus, the vector potential  $A_i$  scales along with the density. In Figure 3 and Figure 4 the initial configurations for the B field are shown for respectively the SOL and the TOR cases. The use of the vector potential guarantees that  $\nabla \cdot \mathbf{B} = 0$ . Thus in the TOR setup, the magnetic field is calculated from  $\mathbf{B} = \nabla \times \mathbf{A}$ . In the SOL setup the magnetic field is calculated from (7), i.e. from the prescribed form of  $\Psi(R, z)$  adopting the corresponding set of parameters

from Table 1. Then equations (A7) and (A8) are used to reconstruct  $B_r$  and  $B_z$ . Since  $\beta_m$  depends on  $\rho(x, z)$ , the magnitude of the magnetic field is rescaled to match a given value of magnetization,  $\beta_m = P/P_m$ , where  $P_m$  is the magnetic pressure. In the TOR case  $P_m$  is initially zero outside the torus, so the rescaling is done only in the inside; in the SOL case  $P_m$  is rescaled outside the torus as well as inside of it. Both simulations have the same initial  $\beta_m$

### 3.3. Input parameters

The computational domain adopted in all the simulations spans from  $R_{\text{in}} = 0.1$  pc to  $R_{\text{out}} = 5$  pc and includes a  $256 \times 32 \times 256$  in  $(r, \phi, z)$  cylindrical grid. The range of  $\phi$  is 0 to  $\pi$  and periodic boundary conditions are imposed. Time from our simulations is often reported in the units of the orbital time at  $R/R_0 = 1$ , where  $R_0 = 1$  pc; that is  $t_0 = 1.6 \times 10^3$  yr. Where appropriate we discuss the results referring to the various variables cast in a non-dimensional form. Adopted parameters are summarized in Table 1 where they are shown divided into two groups: related to the global physical properties of the system, such as BH mass,  $M_{\text{BH}}$  and effective luminosity parameter,  $\Gamma$  and related to the characteristic physical properties of the magnetized gas, such as density and magnetic field. Starting from the initially unperturbed magnetized torus, we performed numerical simulations for several tens to several hundreds  $t_0$ . In case when the radiation pressure on dust is included (Dorodnitsyn et al. 2016), the inner edge of the torus can be plausibly associated with the dust sublimation radius (see Introduction). Models discussed in the current paper do not include dust, and thus the parameter  $R_0$  is a free parameter of the model. In both TOR and SOL setups, characteristic density scale,  $n_0$  is adjusted in the initial setup so that initial tori have similar masses,  $M_t \sim 10^6 M_\odot$  and initial optical depth in the equatorial plane,  $\tau_\perp$ . In the models presented here, we consider only a single value of the parameter describing X-ray heating,  $\Gamma$  - the Eddington ratio.

Model	$M_{\text{BH}}/M_\odot$	$\Gamma$	$f_x$	$R_0$	$R_{\text{in}}$	$\tau_\perp$	$\beta_m$	$a_1$	$a_2$	$b_1$	$\text{Br}_0$	$\text{Br}_1$	$w_0$	$w_1$
TOR	$10^7$	0.5	0.5	1	0.1	10	100	–	–	–	–	–	–	–
SOL	$10^7$	0.5	0.5	1	0.1	5	100	1	1	3	1	6	2	0

Table 1: Parameters adopted for the initial setup.

## 4. Results

### 4.1. General Properties

The time evolution of our models are shown in a series of plots in Figures 5-9 where snapshots of SOL(left) runs are shown against snapshots of TOR (right) runs at times:  $t = 15, 35,$  and  $60$ . The different distributions of large-scale magnetic flux inside and outside the initial torus set the SOL and TOR models on quite different evolution tracks. The different evolution of the two models can be understood in terms of the relative importance of the forces which tend to disperse the gas compared with the forces which confine it. Radiative heating by X-rays produces temperatures which asymptotically approach the Compton temperature,  $\sim 10^7\text{K}$ . This is much greater than the virial temperature at the torus radius, and thus leads to dispersal of the gas in the form of a wind or super-Keplerian outflow.

Magnetic forces can disperse the torus gas due to buoyancy from field which is generated by the MRI instability. The strength of this process depends on the gradient of such forces and hence on the global distribution of fields. A key difference between the two models is that the SOL model evolves and maintains a field strength which is approximately in equipartition with the gas pressure over most of the computational domain. This is true even in regions where the gas density is low, i.e. close to the disk rotational axis and also at large distances from the disk plane. The funnel in the SOL solution is due to the pressure of the large scale poloidal magnetic field  $B_p$  frozen into the gas which permeates the funnel. As the torus evolves, conservation of magnetic flux preserves the shape of the SOL funnel. The SOL model therefore preserves the shape of the gas distribution over much of the time spanned by our simulations. The flow is highly structured: the funnel clearly separates the rest of the torus from smaller  $R$ . The well defined shape of the SOL torus and the increase of density towards the center of the torus creates a shielding layer which preserves the interior from strong X-ray heating.

The TOR model does not evolve equipartition fields outside the initial gas torus region. As the gas in the torus is also rotating differentially the redistribution of angular momentum quickly sets in. The redistribution and loss of angular momentum due to the MRI instability and mass loss through winds both act to change the distribution of gas in the torus. In the TOR solution the shape of the torus after  $t \sim 10t_0$  bears little resemblance to its initial state. Figure 5 shows that in comparison with SOL models the TOR model has much more clumpy and filamentary structure. The funnel formed by the inner edge of the torus is very weak or absent in case of TOR, Both SOL and TOR solutions have low density regions, at smaller radii. In the absence of viscosity or/and magnetic field the rotating gas conserves its specific angular momentum. The relevance of this effect is much reduced in the magnetized



accretion disk in which the angular momentum,  $l$  is redistributed via magnetic stresses.

The pileup of gas at the magnetic funnel shares the same physical mechanism with the “magnetically arrested disk” (Igumenshchev 2008). In the following we will show that this difference, as expected, reduces the mass accretion rate,  $\dot{M}_a$  for SOL solutions. Not only does the SOL solution have piled up gas with higher density, larger optical depth and more complete X-ray screening, but also at any given time the TOR solution has lost more mass and thus has lower average density. In models which include radiation pressure similar behavior is observed due to the action of the radiation alone, which acts to create a well-defined funnel by driving gas above an effective photosphere.

## 4.2. Magnetic Properties

In ideal MHD plasma moves easily along the magnetic field lines while in a direction perpendicular to the magnetic field it can only move while dragging the field. The large-scale poloidal field is dragged towards the center until, approximately  $\rho v_r^2 \sim B_p^2/(8\pi)$ , where  $B_p$  is the poloidal magnetic field. This situation is best seen in the SOL simulation: left panels in Figure 6 which shows the energy of the toroidal field  $E_{m,t} = (8\pi)^{-1} B_\phi^2$ . Correspondingly, Figure 7 shows the energy in the poloidal magnetic field:  $E_{m,p} = (8\pi)^{-1} B_p^2$ . The total magnetic energy density,  $E_m = (8\pi)^{-1}(B_R^2 + B_z^2 + B_\phi^2)$  is highest in and near the torus’s throat and along the axis of symmetry.

Although the TOR simulations initially contained only closed loops of  $B_p$ , toroidal field is quickly and efficiently generated from the poloidal field due to differential rotation. To estimate the production rate of  $B_\phi$  we adopt a full form of the hydromagnetic equation (A4):

$$\partial_t \mathbf{B} = \nabla \times (\mathbf{V} \times \mathbf{B}) - \nabla \times (\eta_m \nabla \times \mathbf{B}), \quad (21)$$

where  $\eta_m$  is the magnetic diffusivity - numerical or real. In the initial distribution of  $B$ ,  $B_R(z=0) = 0$ . Assuming the scaling  $z \ll R$  near the equatorial plane, we obtain  $B_\phi(z \simeq 0) \sim 2\pi \frac{t}{t_{sc}} \frac{R}{z} B_z$ . The field growth is eventually limited by diffusivity, so that  $\partial_t \mathbf{B} \simeq 0$ : From (21) equilibrium  $B_\phi(z \simeq 0) \sim \frac{zR\Omega_K B_z}{\eta_m}$ ; almost everywhere else in the torus  $B_\phi \sim \frac{R^2 \Omega_K B_R}{\eta_m}$ , so that toroidal field is preferentially generated from  $B_r$ .

In the SOL case  $E_{m,t}$  dominates over  $E_{m,p}$  in the funnel region. The TOR solution features a more uniform distribution over the torus region. An interesting feature of both solutions is the presence of low  $E_m$  filaments in the SOL solution and large-scale filaments, of enhances magnetic energy in the TOR case (Figure 6, right). Similar filamentary network

of “voids” and correspondingly high  $E_{m,p}$  regions can be seen in the distribution of  $E_{m,p}$  in Figure 7. The poloidal magnetic field lines,  $B_p$  shown in Figure 7 show a highly randomized behavior expected from the MHD-turbulent medium. Another interesting feature is that in the SOL case most of the poloidal flux is concentrated in the funnel, while in the TOR case - in the filaments. Shearing orbital motion stretches loops of magnetic field while buoyancy and numerical magnetic reconnection produce smaller scale loops. Consequently, regions with the dominant  $B_\phi$  are often intermittent with ones dominated by  $B_p$ . In pressure balance regions where  $E_m$  is high tend to be the low density ones. External radiation preferentially heats these low  $\rho$  and high  $E_m$  patches. The result is a complex pattern in the magnetic energy density distribution. On average,  $E_{m,t} > E_{m,p}$  in the torus. The difference of the magnetic energy densities between the SOL and TOR simulations should be attributed to the aforementioned stabilizing effects of large-scale preexisting poloidal magnetic flux. Comparing Figure 5 to Figure 6 and Figure 7 one can see that in general, in the SOL solutions, regions of high  $E_m$  are the regions of increased density.

### 4.3. Thermodynamics and effects of X-ray heating

Figure 8 shows the distribution of the non-dimensional entropy,  $S = \log P/\rho^\gamma$ . Low entropy gas fills the torus in the SOL case suggesting a smaller extent of mixing during the evolution. Low density, high entropy gas is found near the rotational axis and at larger radii where large scale gas motions occur. The gas piled up near the magnetic funnel in the SOL solution is dense, and correspondingly the entropy is low. At the same time the TOR solution has lost more mass and the radiation heating is more uniform across the range of radii. In the TOR case the entropy distribution shows filamentary structure. Comparing Figure 5 to Figure 6 and Figure 7 one can see that SOL torus has markedly lower entropy than that of the TOR. In the TOR case, entropy traces the filamentary and clumpy structure of the distribution of the average magnetic field.

Different topologies of the initial field results in different levels of MRI- driven stirring of the torus interior. The density near the disk funnel is naturally higher than the density in a smooth disk of the same mass. Shielding depends on the optical depth of the obscuring region,  $\sim \bar{\rho} \delta l$ . In the SOL solution there is little gas in the central hole, and thus the characteristic length scale,  $\delta l$  is smaller, but this is more than compensated by the increase of the density in this region,  $\bar{\rho}$  due to compression of the funnel walls. Correspondingly, the SOL solution shows more efficient shielding from X-rays. Thus, the gas in TOR solution is considerably hotter,  $T \simeq 10^5\text{K}$  than in SOL case,  $T \simeq 10^4\text{K}$ . Near the axis the gas is very hot, almost virialized: in SOL case it is  $T \simeq 10 \times 10^7\text{K}$  and in TOR case it is  $T \simeq 2.5 \times 10^6\text{K}$ .

Angular dependence of the optical depth manifests itself in “ionization cones” (Figure 8, right panels).

Extensive irradiation by X-rays along with the radiative cooling enhance density contrasts produced from MRI-driven convection. Tests of non-irradiated tori show that the conclusions about the effects of magnetic field topology in the SOL vs TOR setups remain qualitatively unchanged. However, X-ray heating and cooling create more turbulent and irregular tori as a result of enhanced convection.

#### 4.4. Velocity and Rotation

The large scale magnetic field in the SOL simulation is effective in smoothing the contrast in specific angular momentum  $l$ , so that this quantity remains close to its local Keplerian value,  $l_k$ . This is not true for the TOR simulations. Figure 9 shows the distribution of  $l(R, z)$ . In the TOR solutions,  $l$  spans the full range, from  $l \sim l_k$  near the inner domain boundary to an approximately half of  $l_k$  at larger  $R$ . The rotation velocity,  $v_\phi$  remains nearly Keplerian inside a significant part of the torus. This is more true close to the equator. In the torus throat most of the low density gas is sub-Keplerian. However, the gas in this region is too dilute to have a noticeable influence on the dynamics and torus. Figure 5 shows an over-dense stream protruding to small  $R$  at late times as the result of the formation of an equatorial, nearly Keplerian, small accretion disk at late stages of the simulation.

Streamlines of the poloidal velocity,  $v_p$  are shown in Figure 5. In the funnel region, the SOL solution has  $v_p$  change from inflow (upper left) to outflow (lower left); inside the main body of the torus, the large scale motion in the SOL solution resembles meridional flows with axial symmetry, but with no equatorial symmetry. In the TOR case the velocity pattern is highly chaotic, without any obvious implied symmetry, though there is a net outflow in the regions near the lower and upper boundaries.

#### 4.5. Obscuration

An important, potentially observable characteristic of a torus is its obscuring properties. The distribution of gas in the computational domain depends on the gas rotation (centrifugal barrier), radiation pressure, and magnetic pressure and tension. When gas has means to shed its angular momentum the centrifugal barrier becomes less relevant. In the case such as ours, when there is no radiation pressure, the role of the large scale magnetic field can be disentangled from other forces shaping the torus. Figure 11 shows column density  $N_{\text{col}}(\theta) =$

$\int_s n(r, \theta) dr$ , as a function of the inclination angle,  $\theta$  measured from the axis of rotation. Each point of a particular color indicates a model at time step,  $t$  i.e. as recorded over the entire simulation time range. There are total of 500 model shown for each setup (SOL: left, or TOR: right).

The qualitative behavior of the solutions is consistent with the Figure 5: The torus confinement by the pressure of the magnetic funnel is quite pronounced in the SOL (left) setup where  $N_{\text{col}}(\theta)$  practically tracks the torus funnel where the gas is piling up. In the TOR setup the distribution of  $N_{\text{col}}(\theta)$  is considerably more uniform. Gas that fills the torus throat provides only negligible obscuration due to its low density. These results demonstrate that the magnetic torus can provide enough obscuration, and which lasts for enough time, to be relevant for the problem of Type II AGN obscuration. supports accretion rate close to the maximum efficiency. From Figure 11 the TOR solution provides larger columns near 90 degrees inclination. The magnetic funnel in the SOL case provides a barrier where the gas is piling up. Thus, at smaller inclinations the SOL disk tends to thin out less at later times, than the TOR disk which does not have such a magnetic funnel.

#### 4.6. Accretion and Wind Mass Loss

Gas can be lost from the system through excretion or wind. Figure 10 shows mass-loss rates through accretion,  $\dot{M}_a$  and through the wind  $\dot{M}_w$  for the SOL(left) and TOR(right) setups. After an initial transient period a quasi-stationary regime of accretion is established in both cases.

Wind mass loss occurs from the upper, lower and right (furthest from the BH) domain boundaries. Mass loss rates from the upper,  $\dot{M}_w^+$  and lower  $\dot{M}_w^-$  dominate the outflow rate while the outflow at the outer  $R$  direction, after initial short increase becomes negligible, less than  $10^{-10} M_\odot \text{ yr}^{-1}$ . An apparent inflow at the right boundary in Figure 5 occurs in the region of a very low density and thus carries very little mass.

Within the time span of the simulation, the torus sheds more mass via  $\dot{M}_w$  than from  $\dot{M}_a$ . Excretion is expected as angular momentum is transferred outwards by both the wind and equatorial outflow. After  $T \sim 2 \times 10^4$  yrs in both runs the mass-loss rate enters a regime in which  $\dot{M}_a$  is fluctuating within a range; in case of SOL:  $\dot{M}_a \simeq 10^{-4} - 10^{-3} M_\odot \text{ yr}^{-1}$ , and TOR:  $\dot{M}_a \simeq 10^{-1} - 3 \times 10^1 M_\odot \text{ yr}^{-1}$ . There is no obvious increasing or decreasing trend in average mass-accretion rate,  $\langle \dot{M}_a \rangle$ . The largest variability scale of the TOR is about  $10^4$  yrs while in the SOL it is much smaller, about  $10^3$  yrs. The variability amplitude in the SOL solutions is generally smaller than in the TOR solutions. In both cases the wind mass-loss

rate,  $\dot{M}_w \simeq 0.01 - 0.1 M_\odot \text{yr}^{-1}$ . Notice that for our model parameters, the Eddington mass-accretion rate,  $\dot{M}_{a,\text{Edd}} \simeq 0.1 M_\odot \text{yr}^{-1}$  where we assumed the efficiency of accretion,  $\epsilon = 0.1$ . The accretion rate in SOL and TOR runs almost always stays below this level with the excess energy removed by winds.

#### 4.7. Comparison to the radiation-pressure supported torus

It is instructive to compare the obscuring properties of the radiation-pressure supported model of the torus from Dorodnitsyn et al. (2016) with predictions of the magnetized torus. In the magnetic case the torus evolves more slowly. In a radiation supported scenario, even at a relatively low radiation energy input of  $L = 0.01 L_{\text{edd}}$ , where  $L_{\text{edd}}$  is the Eddington luminosity, at comparable time since the beginning of the simulations, the torus is significantly more distorted, and windy (see Figure 1 from Dorodnitsyn et al. (2016)). In the SOL or TOR cases an organized wind is much weaker than in the radiation pressure case. The organized pattern of streamlines is found mostly outside the torus, in the region of tenuous plasma.

Comparing properties of magnetic tori with the gas-only and radiation pressure supported tori having similar density scales,  $n_0 = 10^8$ , shows that the torus mass,  $M_t \simeq 10^6 M_\odot$  is similar to the gas-only torus (Dorodnitsyn et al. 2008):  $M_t \simeq 9.3 \times 10^5 M_\odot$ , and in the IR-pressure supported torus  $M_t \simeq 5 \times 10^5 M_\odot$ , (Dorodnitsyn et al. 2016). The mass-loss rates, however, are noticeably higher in the radiation pressure supported model. For example, at a comparable radiation input level,  $\Gamma = 0.3$  the mass-loss rate in the IR-supported torus is  $\dot{M}_w \simeq 0.2 M_\odot \text{yr}^{-1}$ .

### 5. Discussion

We have previously conducted a series of hydrodynamic simulations of the torus designed to better understand its relation to the problem of Seyfert II obscuration and AGN unification as well as its relation to the inner accretion disk. In the current work we report our first results on three-dimensional modeling of magnetized AGN tori exposed to external X-ray heating.

We have found a connection of this problem to the problem of magnetically supported tori in Tokamaks. In the context of Tokamak studies axially-symmetric solutions for a non-rotating, magnetically confined and supported torus made of polytropic gas exists in the literature. Our analytical estimates included the analysis of the solutions to the Grad-

Shafranov equation. We obtain an approximate solution to this problem that demonstrates the possibility of torus be support by the poloidal magnetic field.

In a realistic differentially rotating torus the effects of MRI-driven turbulence are expected to transform the torus into an accretion disk on a dynamical scale. The results from our numerical simulations confirm this expectation. Evidence from this and other simulations (Beckwith et al. 2009; Hawley 2000) suggests that there is an important difference in the outcome of the accretion depending on how the initial magnetic flux is configured.

After the MRI-stirred turbulence sets in, the magnetic field can be viewed as being composed of a regular  $\langle \mathbf{B} \rangle$  and a random  $\mathbf{B}'$  components:

$$\mathbf{B} = \langle \mathbf{B} \rangle + \mathbf{B}', \quad (22)$$

where large scale  $\langle \mathbf{B} \rangle$  is averaged over the statistical ensemble that involves a fluctuating component of the magnetic field,  $\mathbf{B}'$ . If the poloidal component in the initial large-scale  $\mathbf{B}$  is strong enough (as in our SOL setup) previous simulations find that typically  $\langle \mathbf{B}_p \rangle \gtrsim \mathbf{B}'$  and poloidal flux can be accumulated at smaller radii creating a magnetic bundle that impedes accretion. Higher mass fluxes, on the other hand, can enhance mixing between regular and spatially chaotic motions, leading to  $\langle \mathbf{B}_R \rangle \sim \langle \mathbf{B}_z \rangle$ .

It is likely that during a significant episode of accretion, such as may happen during a major merger for example, a significant bundle of large scale magnetic field will be dragged from galactic scales to  $\sim \text{pc}$  scales. Orbital shear and amplification due to flux freezing can further shape the toroidal topology of such a field. If initially most of the  $B_p$ -flux is contained inside a torus then the results of our TOR simulation shows that it will lead to a more spatially chaotic accretion with no magnetic funnel. If significant flux is carried by low-density gas then the results of our SOL simulation shows that an inner magnetic bundle forms.

One should exercise caution in assessing the mechanism of the vertical magnetic field transport. Important collective insight from theoretical and numerical work (Bisnovatyi-Kogan & Lovelace 2007; Beckwith et al. 2009) demonstrate that low density, high  $z$  regions of the disk are the main provider and contributor of the advection of  $B_p$ . The equatorial part of the disk is turbulent and effectively acts as a diamagnetic, rendering frozen in condition irrelevant in this layer and instead allowing matter to slip through the field lines. The accumulation of the poloidal field in this low density regions at smaller radii, creates a magnetically arrested disk (MAD) state. The equatorial flow is still reminiscent of thin, turbulent disk. It is in this thin layer where accretion is mostly happening in the SOL case despite the MAD state of the disk as a whole.

To assess whether or not the MRI-turbulence is numerically resolved, one compares the fastest-growing MRI mode,  $\lambda_{\text{MRI}}$  with the size of the computational grid cell. The safety factor is  $Q_\phi = \lambda_{\text{MRI}}/(R\Delta\phi)$  (e.g. Noble et al. 2010; Sorathia et al. 2012), where  $\Delta\phi$  is the resolution in the  $\phi$  direction. In our notation it is, then  $Q_\phi = 2\pi\sqrt{2}(P/(\rho\beta_m)^{1/2}/(V_k(z=0)\Delta\phi))$ , where  $V_k(z=0)$  is the Keplerian velocity at the equatorial plane. In our simulations  $Q_\phi \simeq 1 - 5$ . Our simulations do not resolve MHD turbulence, thus all the effects associated with magnetic diffusivity  $\eta_m$  should be attributed to the numerical diffusivity of the method. However numerical diffusivity is working towards the same goal as it would be in the case of the effective turbulent diffusivity,  $\eta_m$ : magnetic field diffuses through the accreting gas.

The primary role played by X-ray heating in our simulations is that it enhances entropy contrasts, since the heating is greater in low density regions. In the case of the magnetized inner funnel this leads to enhanced gas evaporation. In previous papers we found that incident X-rays heat the surface of the torus creating a thin overheated layer (“a skin”) which forms a base for an evaporative outflow.

Our simulations include the effects of X-ray heating on the torus gas. The primary role played by X-ray heating is that it enhances entropy contrasts, since the heating is greater in low density regions. In the case of the magnetized inner funnel this leads to enhanced gas evaporation. This paper does not include any of the various other effects of radiation in torus models, including the effects of X-rays and UV in dust grain photodestruction, radiation pressure on dust and on free electrons from UV and on dust from X-rays, dust heating by UV and X-rays and reprocessing into infrared radiation, and the associated pressure from the infrared in a dusty medium. In the models described in this paper all the vertical support comes from the gas and magnetic pressure and tension. The torus vertical support and confinement is the result of the combined action of the gas pressure and the magnetic field pressure and tension. The magnetic field in this scenario is dragged along with the gas, from the galactic scales.

Though the effects of dust and IR are not included in this paper, it is clear that the survival of dust against evaporation by X-rays is a crucial determinant of the dynamical effects of radiation. For instance, if a cold slab of plasma is exposed to unattenuated X-ray and UV radiation, a significant part of such radiation will be absorbed and reprocessed into infrared within a layer of thickness,  $\delta l/R_{1\text{pc}} \simeq 1.3 \times 10^{-3}(n/10^7\text{cm}^{-3})$ . This will create radiation pressure,  $\mathbf{g}_r$  which is primarily in the (spherically) outward direction. The critical Eddington luminosity with respect to dust opacity is  $\Gamma_{\text{IR}} = \alpha \Gamma_{\text{X}}\kappa_d/\kappa_e \simeq 1.25$  for  $M_{\text{BH}} = 10^7 M_\odot$ ,  $L = 0.5L_{\text{edd}}$  and  $\kappa_d = 10\kappa_e$ ; also adopting  $\eta_{\text{X}} = 0.5$  for the fraction of X-ray radiation from the total radiation, and the fraction  $\alpha \simeq 0.5$  of the incident flux is re-emitted outwardly. In our previous papers (Dorodnitsyn et al. 2016; Dorodnitsyn & Kallman 2012)

we have included the effects associated with dust and X-rays: the conversion of X-rays to infrared, and the IR radiation pressure. In the UV the dust opacity is  $\geq 10^2$  times the Thomson opacity, and is correspondingly greater than the X-ray opacity. This results in the absorption of UV in a much thinner 'skin' layer than is the case for X-rays. Far from the disk plane, and at low density, dust evaporation dramatically reduces the vertical component of  $\mathbf{g}_r$ . Close to the disk plane the UV attenuation layer is very thin. The combined pressure of UV radiation and of the pressure of the hot gas on the torus's inside funnel wall pushes the torus outwards, increasing  $R_0$ . Quantitative exploration of these effects will be undertaken in a later paper.

It was also found in Dorodnitsyn et al. (2016) that the formation of a funnel can significantly slow down or even stop accretion via disk viscosity. However, it was found that in this situation accretion can still proceed through capturing the thermally evaporated wind while the accretion disk remains truncated by radiation pressure and heating.

So far we have also neglected non-ideal effects: non-ideal plasma effects can play an important role deep inside the torus where the gas can be cold and neutral and there may be not enough charge-carrying particles. If so, magnetic diffusivity in the equation (21) will be significant, and will allow the magnetic field to effectively slip through the moving fluid. Reduced magnetic dragging means less magnetic force. It is well known that inside a thin accretion disk turbulence can drastically increase the effective diffusivity which renders the transport of the large-scale magnetic fields nearly impossible (Lubow et al. 1994). Very low physical conductivity inside a cold torus will work the same way as high effective diffusivity in accretion disks. On the other hand, it has been shown that radiative layers in the disk Bisnovatyi-Kogan & Lovelace (2007) and corona, and/or low density conductive regions restore the coupling (Bisnovatyi-Kogan & Lovelace 2000; Beckwith et al. 2009). High effective diffusivity inside the torus imply that dynamically important fields should be transported by the hot conductive, diluted gas in which the torus is in pressure equilibrium. The torus will be embedded into such gas and this gas will carry most of the current and magnetic field which in turn will play important role in confining the torus. In our previous simulations X-ray illumination produced large via evaporation of the cold torus. Our assumption that the gas is sufficiently ionized to validate the use of ideal MHD is likely to be applicable whenever the electron fraction exceeds  $\sim 10^{-11}$  Fleming & Stone (2003). The temperatures in our previous IR-driven tori so far are  $\geq 1000$  K. This insures that there is enough charge carrying particles to justify flux-frozen condition.



## 6. Conclusions

We performed numerical simulations of AGN tori threaded by a large scale magnetic field. To illustrate the feasibility of this model, we first studied an illustrative analytical example of the torus that is supported and confined by the strong poloidal, large-scale magnetic field. To isolate the effects of the magnetic support, our three-dimensional numerical model is decisively simplified and includes only large scale magnetic field along with the gas pressure and X-ray heating and cooling. Radiation pressure in any form is neglected. We argue that despite numerous simplifications, the results are in fact in a good agreement with observed properties of AGN tori, and that they validate a scenario in which the torus is a vertically thick accretion disk whose evolution is governed by the magnetic flux supplied from galactic scales. The magnetic field has a major effect on the torus morphology and dynamics:

- We derive an analytic model by considering a generalization of the magnetic topology known in a Tokamak literature as a “Soloviev solution”. Our magnetically confined torus features a poloidal magnetic field which is partly trapped inside the torus where it contributes to its vertical support against gravity. This model also has a significant magnetic flux outside the torus, in the low density gas. We argue that both of these initial states may result from accretion of magnetized gas from galactic scales in which case a dynamically significant magnetic flux can accumulate in the inner regions of AGN as a result of magnetic field dragging from galactic scales.
- Two types of initial magnetic topologies are studied: in the first one (SOL) the initial state is constructed from the modified Soloviev equilibrium. In the second setup (TOR), the magnetic flux is initially contained inside the torus in which case such simulation shares many common features with corresponding simulations of geometrically thick accretion disks. In both cases plasma is exposed to external X-ray illumination, heating and cooling.
- Two main results arrive from these simulations: i) TOR setup evolves into a geometrically thick convective/turbulent accretion disk with  $\langle \mathbf{B}_R \rangle \sim \langle \mathbf{B}_z \rangle$ . The magnetic field provides a mechanism to redistribute angular momentum through MRI turbulence and outflows. ii) The SOL case evolves into a configuration that resembles the arrested disk with a strongly magnetized torus funnel.
- External X-ray irradiation does not qualitatively change the results; however extensive heating does shift the outcome to a more turbulent and irregular torus as a result of enhanced convection.

This work was supported by NASA under Astrophysics Theory Program grants 10-ATP10-0171 and NNX11AI96G.

## REFERENCES

- Antonucci, R. R. J. 1984, *ApJ*, 278, 499
- Antonucci, R. R. J., & Miller, J. S. 1985, *ApJ*, 297, 621
- Avara, M. J., McKinney, J. C., & Reynolds, C. S. 2016, *MNRAS*, 462, 636
- Balbus, S. A., & Hawley, J. F. 1991, *ApJ*, 376, 214
- Barvainis, R. 1987, *ApJ*, 320, 537
- Beck, R. 2011, in *American Institute of Physics Conference Series*, Vol. 1381, American Institute of Physics Conference Series, ed. F. A. Aharonian, W. Hofmann, & F. M. Rieger, 117–136
- Beck, R., & Wiełebinski, R. 2013, *Magnetic Fields in Galaxies*, 641
- Beckert, T., Driebe, T., Hönig, S. F., & Weigelt, G. 2008, *A&A*, 486, L17
- Beckwith, K., Armitage, P. J., & Simon, J. B. 2011, *MNRAS*, 416, 361
- Beckwith, K., Hawley, J. F., & Krolik, J. H. 2009, *ApJ*, 707, 428
- Beskin, V. S. 2009, *MHD Flows in Compact Astrophysical Objects: Accretion, Winds and Jets*, ed. Beskin, V. S.
- Bisnovatyi-Kogan, G. S., & Lovelace, R. V. E. 2000, *ApJ*, 529, 978
- . 2007, *ApJ*, 667, L167
- Bisnovatyi-Kogan, G. S., & Ruzmaikin, A. A. 1974, *Ap&SS*, 28, 45
- Blondin, J. M. 1994, *ApJ*, 435, 756
- Chan, C.-H., & Krolik, J. H. 2016, *ApJ*, 825, 67
- Czerny, B., & Hryniewicz, K. 2011, *A&A*, 525, L8
- Czerny, B., Rózańska, A., & Kuraszkiwicz, J. 2004, *A&A*, 428, 39

- Dorodnitsyn, A., Bisnovaty-Kogan, G. S., & Kallman, T. 2011, *ApJ*, 741, 29
- Dorodnitsyn, A., & Kallman, T. 2012, *ApJ*, 761, 70
- Dorodnitsyn, A., Kallman, T., & Bisnovaty-Kogan, G. S. 2012, *ApJ*, 747, 8
- Dorodnitsyn, A., Kallman, T., & Proga, D. 2008, *ApJ*, 687, 97
- . 2016, *ApJ*, 819, 115
- Elitzur, M., & Shlosman, I. 2006, *ApJ*, 648, L101
- Emmering, R. T., Blandford, R. D., & Shlosman, I. 1992, *ApJ*, 385, 460
- Everett, J. E. 2005, *ApJ*, 631, 689
- Fleming, T., & Stone, J. M. 2003, *ApJ*, 585, 908
- Fromang, S., & Papaloizou, J. 2007, *A&A*, 476, 1113
- Fukumura, K., Kazanas, D., Contopoulos, I., & Behar, E. 2010, *ApJ*, 723, L228
- Gammie, C. F. 2001, *ApJ*, 590, 174
- Goodman, J. 2003, *MNRAS*, 339, 937
- Guan, X., Gammie, C. F., Simon, J. B., & Johnson, B. M. 2009, *ApJ*, 694, 1010
- Hawley, J. F. 2000, *ApJ*, 528, 462
- Hawley, J. F., Gammie, C. F., & Balbus, S. A. 1995, *ApJ*, 440, 742
- Hawley, J. F., & Krolik, J. H. 2001, *ApJ*, 548, 348
- Hawley, J. F., Richers, S. A., Guan, X., & Krolik, J. H. 2013, *ApJ*, 772, 102
- Hönig, S. F., Kishimoto, M., Antonucci, R., Marconi, A., Prieto, M. A., Tristram, K., & Weigelt, G. 2012, *ApJ*, 755, 149
- Hopkins, P. F., Hayward, C. C., Narayanan, D., & Hernquist, L. 2012, *MNRAS*, 420, 320
- Hopkins, P. F., Hernquist, L., Martini, P., Cox, T. J., Robertson, B., Di Matteo, T., & Springel, V. 2005, *ApJ*, 625, L71
- Hopkins, P. F., & Quataert, E. 2010, *MNRAS*, 407, 1529
- Igumenshchev, I. V. 2008, *ApJ*, 677, 317

- Igumenshchev, I. V., Narayan, R., & Abramowicz, M. A. 2003, *ApJ*, 592, 1042
- Jaffe, W., et al. 2004, *Nature*, 429, 47
- Kallman, T. R., & Bautista, M. A. 2001, *ApJS*, 133, 221
- Keating, S. K., Everett, J. E., Gallagher, S. C., & Deo, R. P. 2012, *ApJ*, 749, 32
- Kishimoto, M., Hönig, S. F., Antonucci, R., Barvainis, R., Kotani, T., Tristram, K. R. W., Weigelt, G., & Levin, K. 2011, *A&A*, 527, A121
- Kishimoto, M., et al. 2013, *ApJ*, 775, L36
- Konigl, A., & Kartje, J. F. 1994, *ApJ*, 434, 446
- Krolik, J. H. 2007, *ApJ*, 661, 52
- Lawrence, A., & Elvis, M. 2010, *ApJ*, 714, 561
- Leontovich, A. M. A., ed. 1975, *Reviews of Plasma Physics*, Vol. 6, *Reviews of Plasma Physics*, Volume 6
- López-Gonzaga, N., & Jaffe, W. 2016, *A&A*, 591, A128
- Lovelace, R. V. E., Romanova, M. M., & Biermann, P. L. 1998, *A&A*, 338, 856
- Lubow, S. H., Papaloizou, J. C. B., & Pringle, J. E. 1994, *MNRAS*, 267, 235
- Lynden-Bell, D., & Kalnajs, A. J. 1972, *MNRAS*, 157, 1
- Maschke, E. K., & Perrin, H. 1980, *Plasma Physics*, 22, 579
- McKinney, J. C., Tchekhovskoy, A., & Blandford, R. D. 2012, *MNRAS*, 423, 3083
- Meisenheimer, K., et al. 2007, *A&A*, 471, 453
- Narayan, R., Igumenshchev, I. V., & Abramowicz, M. A. 2003, *PASJ*, 55, L69
- Netzer, H., & Laor, A. 1993, *ApJ*, 404, L51
- Noble, S. C., Krolik, J. H., & Hawley, J. F. 2010, *ApJ*, 711, 959
- Paczynski, B. 1978, *Acta Astron.*, 28, 91
- Papaloizou, J. C. B., & Pringle, J. E. 1984, *MNRAS*, 208, 721

- Phinney, E. S. 1989, in NATO ASIC Proc. 290: Theory of Accretion Disks, ed. F. Meyer, 457–+
- Pier, E. A., & Krolik, J. H. 1993, *ApJ*, 418, 673
- Pogge, R. W., & De Robertis, M. M. 1993, *ApJ*, 404, 563
- Poncelet, A., Perrin, G., & Sol, H. 2006, *A&A*, 450, 483
- Raban, D., Jaffe, W., Röttgering, H., Meisenheimer, K., & Tristram, K. R. W. 2009, *MNRAS*, 394, 1325
- Rafikov, R. R. 2009, *ApJ*, 704, 281
- Rieke, G. H., & Lebofsky, M. J. 1981, *ApJ*, 250, 87
- Rowan-Robinson, M. 1977, *ApJ*, 213, 635
- Sanders, D. B., Phinney, E. S., Neugebauer, G., Soifer, B. T., & Matthews, K. 1989, *ApJ*, 347, 29
- Sano, T., Inutsuka, S.-i., Turner, N. J., & Stone, J. M. 2004, *ApJ*, 605, 321
- Shi, J., & Krolik, J. H. 2008, *ApJ*, 679, 1018
- Shi, J.-M., Stone, J. M., & Huang, C. X. 2016, *MNRAS*, 456, 2273
- Shlosman, I., Begelman, M. C., & Frank, J. 1990, *Nature*, 345, 679
- Shlosman, I., Frank, J., & Begelman, M. C. 1989, *Nature*, 338, 45
- Simon, J. B., Hawley, J. F., & Beckwith, K. 2009, *ApJ*, 690, 974
- Skinner, M. A., & Ostriker, E. C. 2010, *ApJS*, 188, 290
- Sorathia, K. A., Reynolds, C. S., Stone, J. M., & Beckwith, K. 2012, *ApJ*, 749, 189
- Spruit, H. C. 1996, in NATO Advanced Science Institutes (ASI) Series C, Vol. 477, NATO Advanced Science Institutes (ASI) Series C, ed. R. A. M. J. Wijers, M. B. Davies, & C. A. Tout, 249–286
- Stone, J. M., Gardiner, T. A., Teuben, P., Hawley, J. F., & Simon, J. B. 2008, *ApJS*, 178, 137
- Suganuma, M., et al. 2006, *ApJ*, 639, 46

- Suzuki, T. K., & Inutsuka, S.-i. 2014, *ApJ*, 784, 121
- Tassoul, J. 1978, *Theory of rotating stars*, ed. Tassoul, J.-L. (Princeton Series in Astrophysics, Princeton: University Press, 1978)
- Tristram, K. R. W., Burtscher, L., Jaffe, W., Meisenheimer, K., Hönig, S. F., Kishimoto, M., Schartmann, M., & Weigelt, G. 2014, *A&A*, 563, A82
- Tristram, K. R. W., & Schartmann, M. 2011, *A&A*, 531, A99
- Tristram, K. R. W., et al. 2007, *A&A*, 474, 837
- Weigelt, G., et al. 2012, *A&A*, 541, L9
- Wilson, A. S. 1996, *Vistas in Astronomy*, 40, 63
- Wittkowski, M., Kervella, P., Arsenault, R., Paresce, F., Beckert, T., & Weigelt, G. 2004, *A&A*, 418, L39
- Zakamska, N. L., et al. 2005, *AJ*, 129, 1212

### A. Appendix: Grad-Shafranov equation(s) for the torus.

In cylindrical coordinates, equation of motion (2) reads

$$\rho (\partial_t + \mathbf{v} \cdot \nabla) \mathbf{v} = -\nabla P + \mathbf{F}_m - \rho \frac{G M_{\text{BH}}}{r^2} \hat{\mathbf{r}}. \quad (\text{A1})$$

The Lorentz force  $\mathbf{F}_m$  reads:

$$\mathbf{F}_m = \frac{\mathbf{J} \times \mathbf{B}}{c}, \quad (\text{A2})$$

where  $\mathbf{B}$  is the magnetic field and the current density,  $\mathbf{J}$  is found from:

$$\mathbf{J} = \frac{c}{4\pi} \nabla \times \mathbf{B}. \quad (\text{A3})$$

Ideal MHD implies that  $\mathbf{B}$  satisfies the hydromagnetic equation:

$$\partial_t \mathbf{B} = \nabla \times (\mathbf{V} \times \mathbf{B}). \quad (\text{A4})$$

It is convenient, instead of the magnetic field,  $\mathbf{B}$  to adopt a vector potential,  $\mathbf{A}$ :

$$\mathbf{B} = \nabla \times \mathbf{A}. \quad (\text{A5})$$

Axial symmetry allows to describe all of the magnetic properties via a single flux function,  $\Psi \sim A_\phi$ , instead of the three components of  $\mathbf{B}$ . The flux function is defined from the following equation:

$$\Psi(R, z) = \frac{1}{2\pi} \int \mathbf{B} \cdot \mathbf{n} ds = \frac{1}{2\pi} \int \nabla \times \mathbf{A} \cdot \mathbf{n} ds = \frac{1}{2\pi} \int_0^{2\pi} A_\phi \cdot \hat{\phi} dl = A_\phi R, \quad (\text{A6})$$

where  $\mathbf{n}$  is the normal vector to the equatorial plane,  $l$  is the element of length of the circle of the radius  $R$ . From (A5) and (A6) the  $r$ -, and  $\phi$ -components of the magnetic field read:

$$B_r = -\partial_z A_\phi = -\frac{1}{R} \partial_z \Psi, \quad (\text{A7})$$

$$B_z = -\frac{1}{R} \partial_R \Psi. \quad (\text{A8})$$

From (A7),(A8) one has:

$$\mathbf{B} = \frac{I}{R} \hat{\phi} + \frac{\nabla \Psi \times \hat{\phi}}{R}, \quad (\text{A9})$$

where  $I = RB_\phi$  is the poloidal current. We assume that the gas can be described by a polytropic equation of state:

$$P = K \rho^\gamma, \quad (\text{A10})$$

where  $\gamma = 1 + \frac{1}{n}$ , where  $n$  is the polytropic index, and  $K$  is constant. The later implies that entropy is constant as well. Instead of pressure,  $P$  it is more convenient, to use enthalpy,  $H$ , as for the equation of state (A10) it can be cast in the form:

$$H = \frac{\gamma}{\gamma - 1} \frac{P}{\rho}. \quad (\text{A11})$$

The  $r$ –, and  $\phi$ –components of the equation of motion (A1) transform as follows:

$$\rho \partial_R(H + \phi) = \left( \frac{J_\phi}{cR} - \frac{I(\Psi) I(\Psi)'}{4\pi R^2} \right) \partial_R \Psi + \rho \frac{v_\phi^2}{R}, \quad (\text{A12})$$

$$\rho \partial_z(H + \phi) = \left( \frac{J_\phi}{cR} - \frac{I(\Psi) I(\Psi)'}{4\pi R^2} \right) \partial_z \Psi, \quad (\text{A13})$$

where  $v_\phi$  is the angular velocity of the gas; prime denotes the differentiation over  $\Psi$ , and we also used the relation  $dP = \rho dH$  which follows from (A10) and (A11). Equations (A12), (A13) can be combined into a single Grad-Shafranov equation which was in fact initially derived by Soloviev (Leontovich 1975). The  $\phi$ –component of the current density,  $J_\phi$  is found from (A3):

$$J_\phi = \frac{c}{4\pi} (\partial_z B_r - \partial_R B_z) = -\frac{c}{4\pi} \Delta^* \Psi, \quad (\text{A14})$$

where the “pseudo-Laplacian”,  $\Delta^*$  is defined by the following relation:

$$\Delta^* \Psi = \partial_z \partial_z \Psi + R \partial_R \left( \frac{1}{R} \partial_R \Psi \right). \quad (\text{A15})$$

From (9) and (A12)- (A15) the Grad-Shafranov equation is obtained:

$$\rho (\nabla B_r + \Omega R^2 \nabla \Omega) = -\frac{1}{4\pi R^2} (\nabla^* \Psi + I I) \nabla \Psi. \quad (\text{A16})$$

From (A16) now, an expression for  $\rho$  can be obtained:

$$\begin{aligned} \rho &= -\frac{1}{4\pi R^2} \frac{\nabla^* \Psi + I I'}{\partial_R (\text{Br}(\Psi) + \frac{\Omega^2 R^2}{2}) - \Omega^2 R} \partial_R \Psi = -\frac{1}{4\pi R^2} \frac{\nabla^* \Psi + I I'}{\partial_z (\text{Br}(\Psi) + \frac{\Omega^2 R^2}{2})} \partial_z \Psi \\ &= -\frac{1}{4\pi R^2} \frac{\nabla^* \Psi + I I'}{\text{Br}'(\Psi) + \Omega(\Psi) \Omega'(\Psi) R^2}. \end{aligned} \quad (\text{A17})$$

Assuming  $\text{Br} = \Omega = 0$ , and assuming  $\frac{dP(\Psi)}{d\Psi} = 0$  one can find a Soloviev solution (7) by direct substitution and balancing the remaining free parameters.



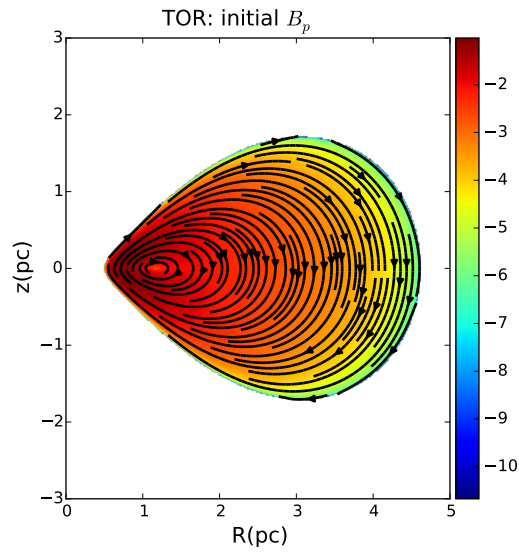


Fig. 4.— Initial magnetic field in the TOR simulation. Color plot:  $B_p^2/8\pi$ ; streamlines:  $\mathbf{B}_p$ . Axes: z: distance from equatorial plane in parsecs; R: distance from the BH in parsecs.

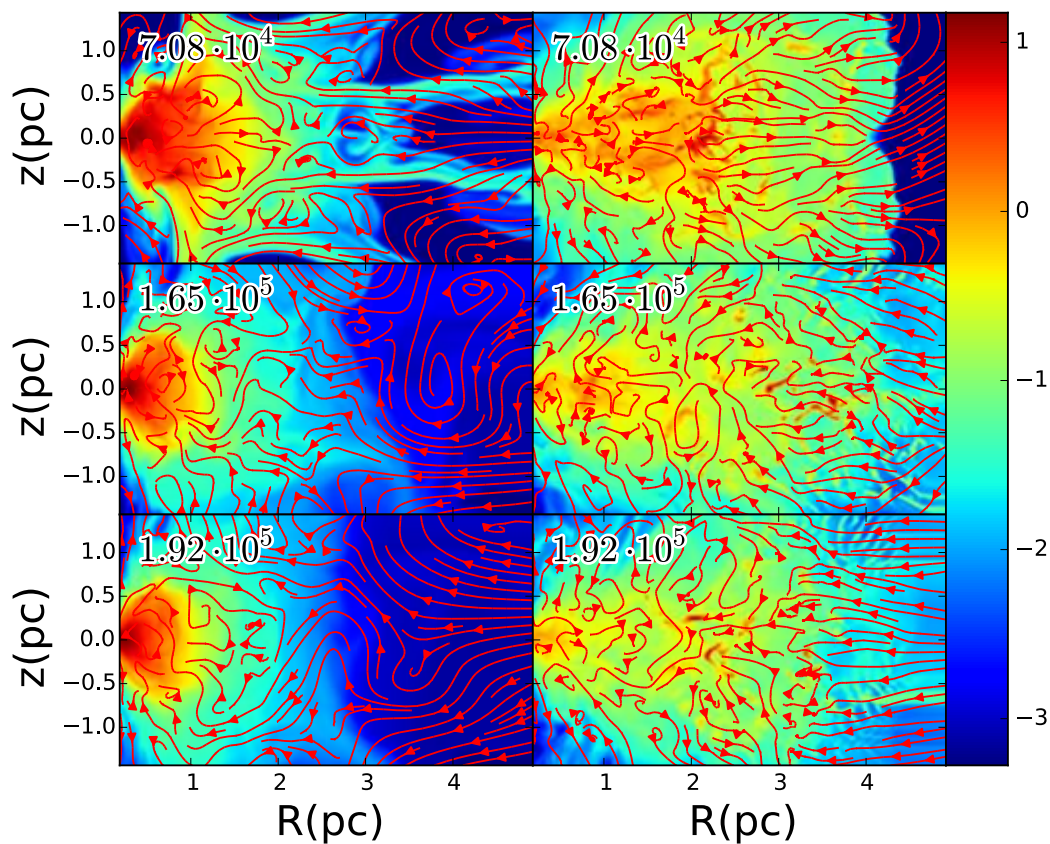


Fig. 5.— Color plot of the density,  $\log \rho$  for  $L_x = 0.25 L_{\text{edd}}$ , ( $\Gamma = 0.5$ ,  $f_x = 0.5$ ), superimposed with the velocity stream lines. Shown are different times given in years. Left column: SOL models; right column: TOR models. Axes: horizontal:  $z$ : distance from equatorial plane in parsecs;  $R$ : distance from the BH in parsecs.

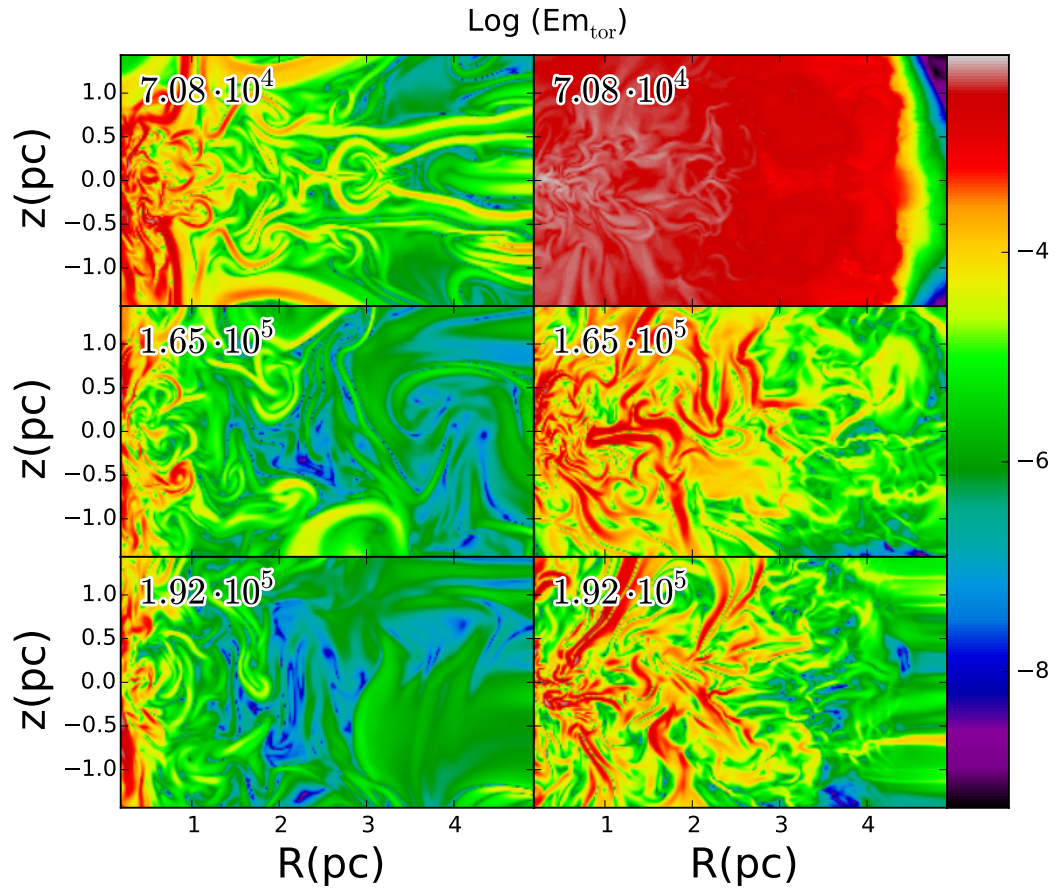


Fig. 6.— Energy from toroidal magnetic field  $E_{m,t} = (8\pi)^{-1} B_\phi^2$ ; other notation is the same as in Figure 5.

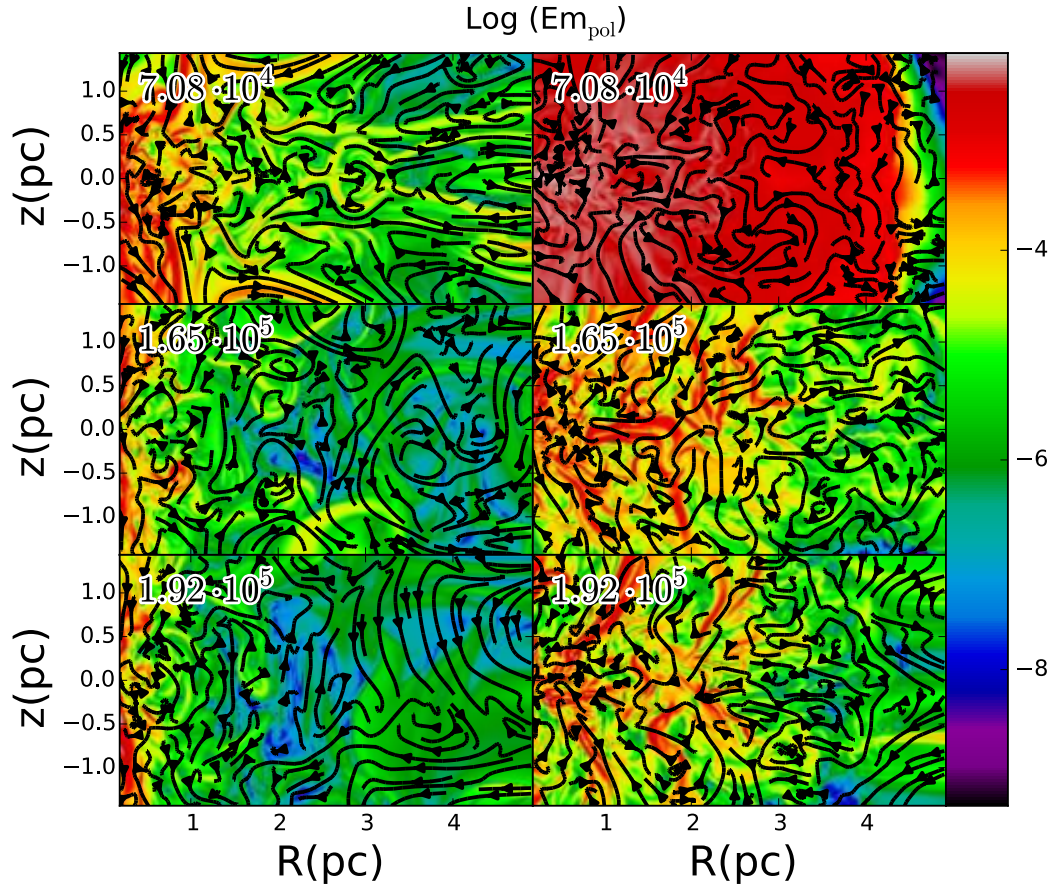


Fig. 7.— Energy from poloidal magnetic field  $E_{m,p} = (8\pi)^{-1} B_p^2$  with streamlines of  $B_p$ ; other notation is the same as in Figure 5.

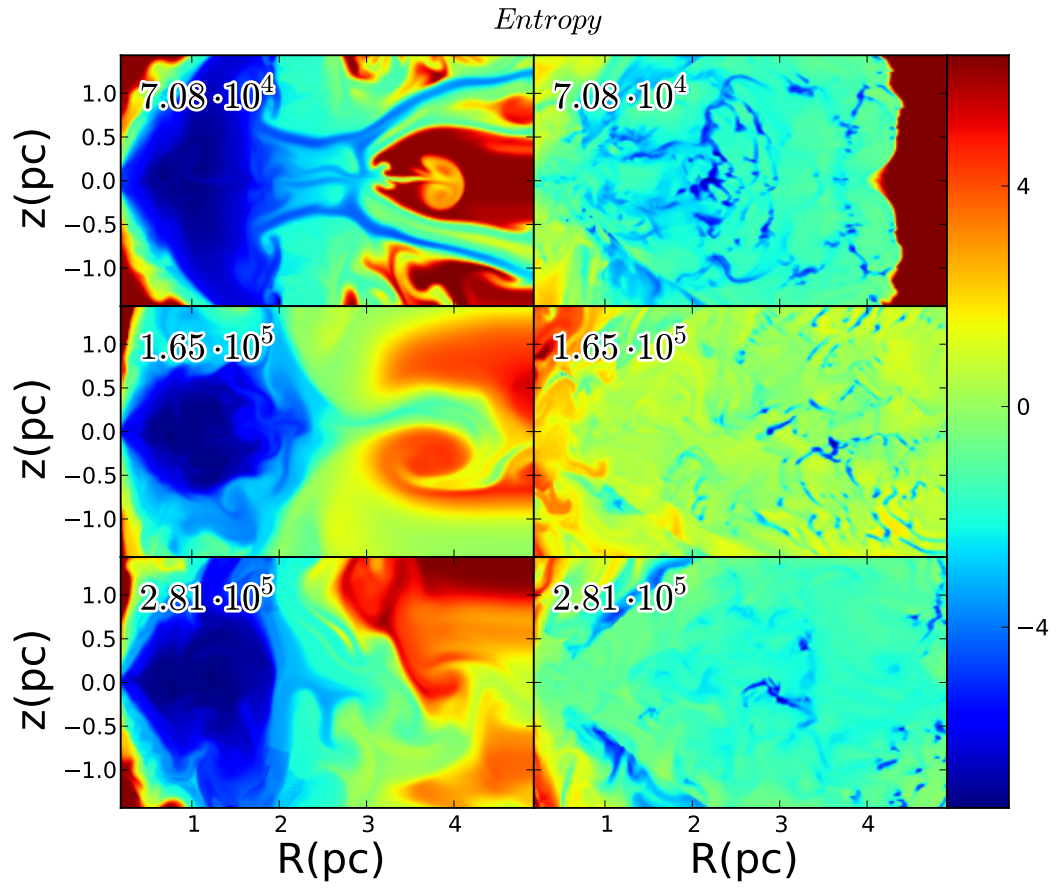


Fig. 8.— Specific entropy; other notation is the same as in Figure 5.



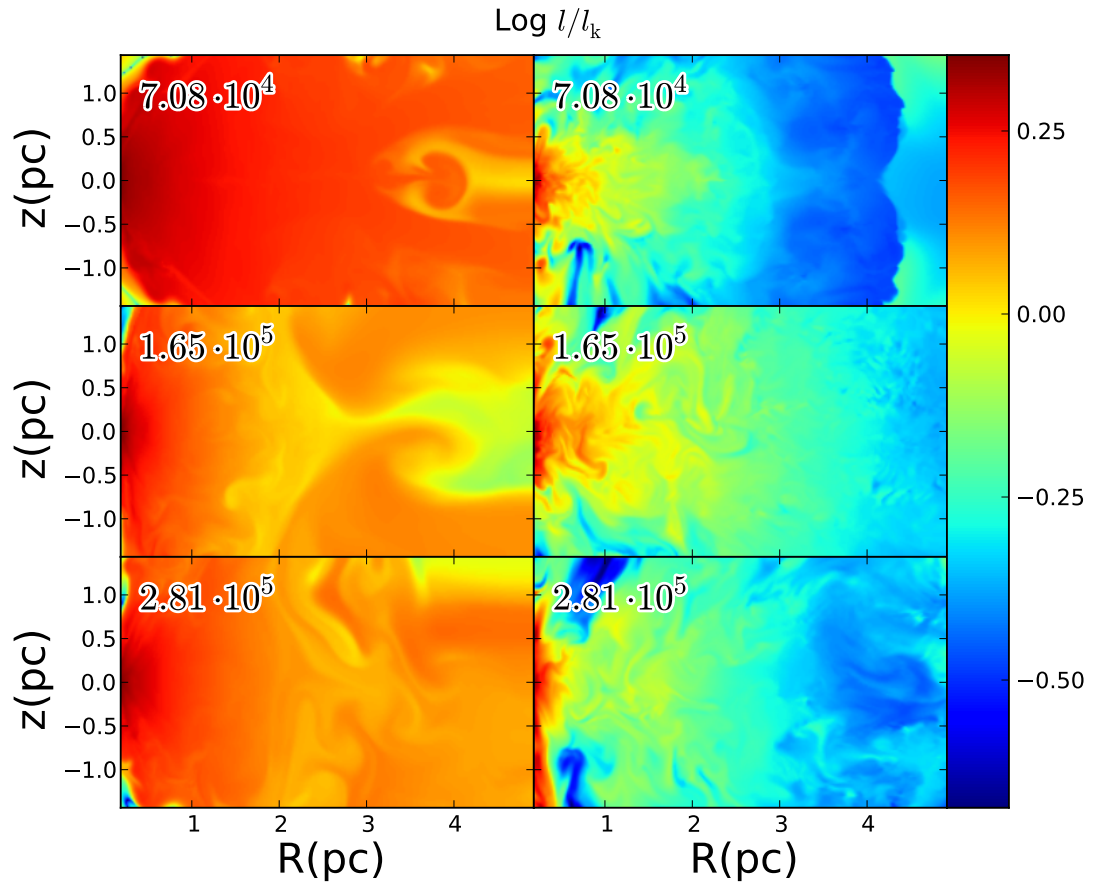


Fig. 9.— Angular momentum:  $l/l_k$ , where  $l_k$  is the Keplerian angular momentum.; other notation is the same as in Figure 5.

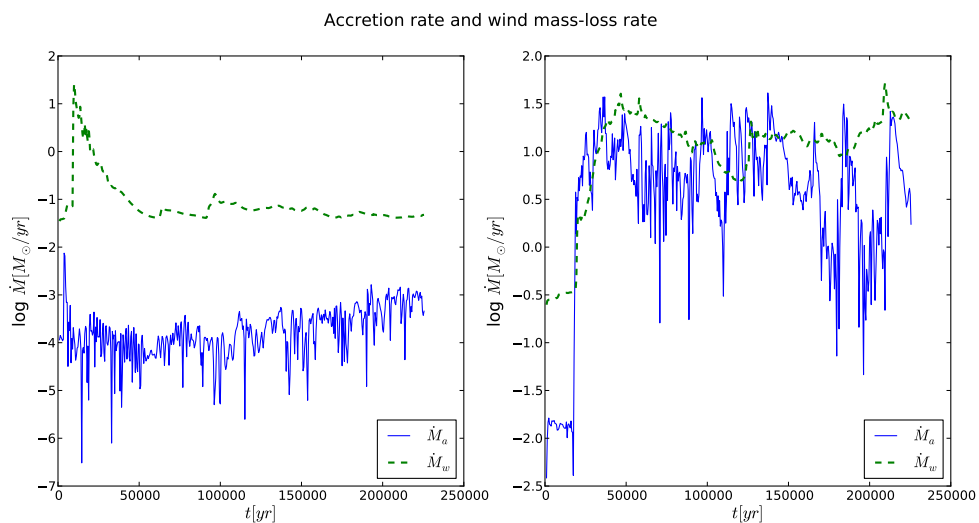


Fig. 10.— Accretion rate,  $\dot{M}_a$  and the total wind mass-loss rate,  $\dot{M}_w$  versus time for two different initial setups: Left: SOL; right: TOR

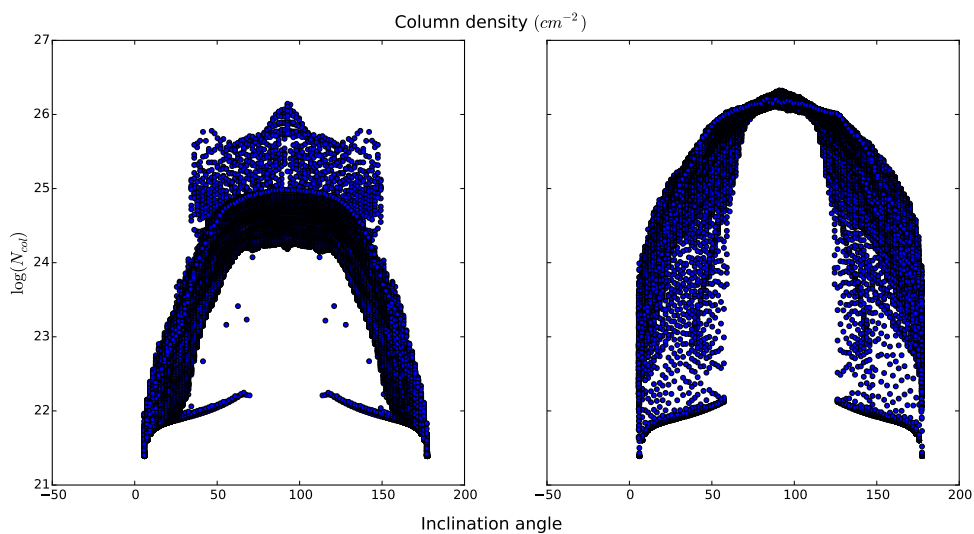


Fig. 11.— Scatter plot showing the logarithm of the column density,  $N_{\text{col}}(\text{cm}^{-2})$ . Each recorded simulation time is represented by a point. Left: SOL; right: TOR